Astronomy & Astrophysics manuscript no. output
April 23, 2026

Euclid: Quick Data Release (Q1) – Dual active galactic nuclei in low-mass galaxies⋆

M. Mezcua⋆⋆[1,2], B. Laloux[3,4], M. Scialpi[5,6,7], M. Siudek[1,8,9], A. Eróstegui[10], F. Ricci[11,12], T. Matamoro Zatarain[13], S. Visser[14], H. J. A. Rottgering[14], C. M. Gutierrez[8,9], A. Feltre[7], L. Bisigello[15], C. Saulder[4,16], L. Ulivi[6,5,7], J. H. Knapen[8,9], H. Domínguez Sánchez[17], G. Zamorani[18], K. Rubinur[19], J. Calhau[3], L. Spinoglio[20], F. Shankar[21], D. Stern[22], R. Pucha[23], A. Viitanen[24,25,12], B. Altieri[26], S. Andreon[27], N. Auricchio[18], M. Baldi[28,18,29], S. Bardelli[18], P. Battaglia[18], A. Biviano[30,31], M. Brescia[32,3], S. Camera[33,34,35], G. Cañas-Herrera[36,14], V. Capobianco[35], C. Carbone[37], J. Carretero[38,39], M. Castellano[12], G. Castignani[18], S. Cavuoti[3,40], K. C. Chambers[41], A. Cimatti[42], C. Colodro-Conde[8], G. Congedo[36], C. J. Conselice[43], L. Conversi[44,26], Y. Copin[45], F. Courbin[46,47,10], H. M. Courtois[48], M. Cropper[49], H. Degaudenzi[25], G. De Lucia[30], C. Dolding[49], H. Dole[50], F. Dubath[25], X. Dupac[26], M. Farina[20], R. Farinelli[18], F. Faustini[12,51], S. Ferriol[45], M. Frailis[30], E. Franceschi[18], M. Fumana[37], S. Galeotta[30], K. George[52], B. Gillis[36], C. Giocoli[18,29], J. Gracia-Carpio[4], A. Grazian[15], F. Grupp[4,16], S. V. H. Haugan[19], J. Hoar[26], H. Hoekstra[14], W. Holmes[22], I. M. Hook[53], F. Hormuth[54], A. Hornstrup[55,56], K. Jahnke[57], M. Jhabvala[58], S. Kermiche[59], B. Kubik[45], M. Kümmel[16], M. Kunz[60], H. Kurki-Suonio[61,62], A. M. C. Le Brun[63], S. Ligori[35], P. B. Lilje[19], V. Lindholm[61,62], I. Lloro[64], G. Mainetti[65], D. Maino[66,37,67], E. Maiorano[18], O. Mansutti[30], O. Marggraf[68], M. Martinelli[12,69], N. Martinet[70], F. Marulli[71,18,29], R. J. Massey[72], E. Medinaceli[18], S. Mei[73,74], Y. Mellier⋆⋆⋆[75,76], M. Meneghetti[18,29], E. Merlin[12], G. Meylan[77], A. Mora[78], M. Moresco[71,18], L. Moscardini[71,18,29], C. Neissner[79,39], R. C. Nichol[80], S.-M. Niemi[81], C. Padilla[79], S. Paltani[25], F. Pasian[30], K. Pedersen[82], W. J. Percival[83,84,85], V. Pettorino[81], S. Pires[86], G. Polenta[51], M. Poncet[87], L. A. Popa[88], L. Pozzetti[18], F. Raison[4], A. Renzi[89,90], J. Rhodes[22], G. Riccio[3], E. Romelli[30], M. Roncarelli[18], E. Rossetti[28], B. Rusholme[91], R. Saglia[16,4], Z. Sakr[92,93,94], D. Sapone[95], B. Sartoris[16,30], M. Sauvage[86], M. Schirmer[57], P. Schneider[68], A. Secroun[59], G. Seidel[57], S. Serrano[2,96,1], E. Sihvola[24], P. Simon[68], C. Sirignano[89,90], G. Sirri[29], L. Stanco[90], J. Steinwagner[4], P. Tallada-Crespí[38,39], A. N. Taylor[36], I. Tereno[97,98], N. Tessore[49], S. Toft[99,100], R. Toledo-Moreo[101], F. Torradeflot[39,38], I. Tutusaus[1,2,93], L. Valenziano[18,102], J. Valiviita[61,62], T. Vassallo[30], Y. Wang[91], J. Weller[16,4], A. Zacchei[30,31], F. M. Zerbi[27], I. A. Zinchenko[103], E. Zucca[18], J. García-Bellido[104], M. Huertas-Company[8,105,106], J. Macias-Perez[107], J. Martín-Fleitas[108], and V. Scottez[75,109]

(Affiliations can be found after the references)

April 23, 2026

ABSTRACT

Dual active galactic nuclei (AGNs) are expected in hierarchical galaxy evolution models, in which low-mass galaxies merge to build more massive ones. While observational evidence for dual AGNs is growing in massive galaxies, no clear detection has yet been found in the low-mass regime. We used photometry and spectroscopy from the first *Euclid* Quick Data Release, combined with a collection of multi-wavelength data from the Dark Energy Spectroscopic Instrument (DESI), the LOw-Frequency ARray (LOFAR) high band antenna, and counterparts in X-ray and mid-infrared catalogues to identify dual AGNs at redshift $z \lesssim 1$. Focusing on low-mass galaxies with stellar masses below $10^{10}\,M_{\odot}$, we find nine dual AGN candidates with projected separations ranging from ∼20 to 51 kpc. We also find 49 dual AGN candidates in more massive galaxies. We derive a dual AGN fraction of 0.1% for the low-mass galaxies and estimate that these systems likely trace a population of progenitor black hole pairs that may evolve into bound binaries and eventually coalesce, emitting gravitational waves in the LISA band. These results constitute the first sample of spectroscopically confirmed dual AGN candidates in low-mass galaxies and have important implications for models in which supermassive black holes grow from lower-mass black holes located in low-mass galaxies, as well as for predictions of gravitational waves from low-mass binary black holes.

Key words. Galaxies: active – Catalogues – Surveys

1. Introduction

Supermassive black holes (SMBHs) are ubiquitous in massive galaxies [stellar mass $\log_{10}(M_*/M_{\odot}) > 10$], from the local to the high-redshift (z) Universe. Yet, how they form and grow is still a matter of debate (see review by Alexander et al. 2025). The discovery of SMBHs at $z \sim 6$–10 (e.g. Bogdán et al. 2024;

⋆ This paper is published on behalf of the Euclid Consortium.
⋆⋆ e-mail: mezcua@ice.csic.es
⋆⋆⋆ Deceased

Maiolino et al. 2024) suggests they grow from lower-mass seed black holes with 100–10^6 $M_\odot$ formed in the early Universe (see reviews by Volonteri 2010; Mezcua 2017; Greene et al. 2020). Galaxy mergers are thought to play a significant role by funnelling gas towards galaxy centres, triggering active galactic nucleus (AGN) activity and thus black hole growth (e.g. Hopkins et al. 2006; Wild et al. 2007). The AGNs at the centres of merging galaxies also evolve during the merger, progressing through a dual and then a binary (gravitationally bound) phase, until they coalesce and emit gravitational waves. Indeed, hundreds to thousands of dual AGNs have been identified in massive galaxies based on optical, infrared, radio, or X-ray diagnostics (see the compilation by Pfeifle et al. 2024) and with separations ranging from less than 1 kpc (e.g. Komossa et al. 2003; Koss et al. 2023) to more than 50 kpc (Liu et al. 2011; Koss et al. 2012; De Rosa et al. 2019, 2023; Mannucci et al. 2022, 2023; Ciurlo et al. 2023; Scialpi et al. 2024; Perna et al. 2025; Ulivi et al. 2025; Euclid Collaboration: Fabricius et al. 2026).

The presence of AGNs in dwarf or low-mass galaxies [$\log_{10}(M_*/M_\odot) \lesssim 10$][1] is increasingly becoming a commonly observed phenomenon (e.g. Reines et al. 2013; Mezcua et al. 2018, 2019, 2023, 2024; Salehirad et al. 2022; Siudek et al. 2023; Mezcua & Domínguez Sánchez 2020, 2024; Pucha et al. 2025), and dwarf galaxies are often found to be interacting or merging (e.g. Paudel et al. 2018). Nevertheless, studies on merger-triggered AGN activity in the dwarf galaxy regime are scant and inconclusive (e.g. Kaviraj et al. 2019; Bichang'a et al. 2024; Mićić et al. 2024; Eróstegui et al. 2025), and no spectroscopically confirmed dual AGN has yet been found in low-mass galaxies.

Local dwarf galaxies are expected to host the relics of those early-Universe seed black holes that did not grow into SMBHs (e.g. Mezcua 2017; Greene et al. 2020; Reines 2022). Therefore, understanding whether galaxy mergers can trigger seed black hole growth in low-mass galaxies, and whether dual AGNs form at all and evolve into binary black holes that coalesce, can have major implications for models of seed black hole formation and evolution (e.g. Deason et al. 2014; Mezcua 2019).

Thanks to its superb photometric sensitivity in the optical and near-infrared regimes, the *Euclid* mission offers an exciting opportunity for identifying faint merger signatures in the dwarf galaxy regime and better constraining merging galaxy properties (i.e. stellar masses) when performing spectral energy distribution (SED) fitting (Euclid Collaboration: Laloux et al. 2026). In addition, *Euclid*'s near-infrared spectrometer provides the possibility to identify broad-line AGNs whose optical emission lines are obscured by dust (Lamperti et al. 2017), making the observatory ideal for investigating dual AGNs in galaxy mergers.

In this paper we used the first Quick Data Release (Q1) of the *Euclid* mission (Euclid Collaboration: Aussel et al. 2025) to identify dual AGNs and galaxy mergers across mass scales, with the focus on the low-mass regime. We identify nine dual AGN candidates in low-mass galaxies, the first sample of its kind. The data analysis is reported in Sect. 2, the results and discussion in Sect. 3, and the conclusions in Sect. 4. We assumed a Λ Cold Dark Matter cosmology with $H_0 = 70\,\mathrm{km\,s^{-1}\,Mpc^{-1}}$, $\Omega_\mathrm{m} = 0.3$, and $\Omega_\Lambda = 0.7$.

[1] Both the term 'dwarf' versus 'low-mass' and the stellar mass threshold adopted to define this regime suffer from a lack of consensus in the literature. We adopt here the same definition [$\log_{10}(M_*/M_\odot) \lesssim 10$] as in some recent work on dwarf galaxy mergers and AGNs (e.g. Manzano-King & Canalizo 2020; Bichang'a et al. 2024; Eróstegui et al. 2025), but refer to our sources as 'low-mass' to be conservative.

2. Data and analysis

The *Euclid* mission provides high-spatial-resolution (0.″18; Euclid Collaboration: Cropper et al. 2025) optical imaging with the visible instrument (VIS; I_E covers $\lambda = 0.53$–$0.92\,\mu$m) and low-resolution near-infrared spectroscopy and photometry ($R \sim 450$ for objects with a diameter of 0.″5) with the Near-infrared Spectrometer and Photometer (NISP; with Y_E, J_E, and H_E covering $\lambda = 0.95$–$2.02\,\mu$m; Euclid Collaboration: Schirmer et al. 2022; Euclid Collaboration: Jahnke et al. 2025) of millions of galaxies out to $z = 6$ (Euclid Collaboration: Mellier et al. 2025). The Euclid Wide Survey (EWS; Euclid Collaboration: Scaramella et al. 2022) will cover over 14 000 deg^2 to a depth of $I_\mathrm{E} = 26.2$ (5σ point-like source). The Euclid Deep Survey (EDS) will observe three different areas, the so-called Euclid Deep Fields (EDF-North, EDF-N; EDF-South, EDF-S; and EDF-Fornax, EDF-F) covering over 53 deg^2 to a depth of $I_\mathrm{E} = 28.2$ (Euclid Collaboration: Mellier et al. 2025).

In this study, we used Q1 data (Euclid Quick Release Q1 2025), which constitutes a first visit to the EDFs, covering a total area of 63.1 deg^2 at the depth of the EWS (Euclid Collaboration: Aussel et al. 2025). We used the EDF-N, since it is the only field that overlaps with the Dark Energy Spectroscopic Instrument (DESI) Early Data Release (EDR; DESI Collaboration et al. 2024), which provides robust spectroscopic redshifts (see Euclid Collaboration: Matamoro Zatarain et al. 2025 for details; hereafter EC:MZ25). Starting from the 1.1×10^7 sources in the *Euclid* Q1 EDF-N and after applying the quality cuts specified in Sect. 2.1.1 of EC:MZ25, a total of 24 922 sources were found to have a DESI spectroscopic counterpart. Crossmatching was done using a conservative 0.″5 radius, corresponding to approximately six times the DESI fibre positioning accuracy (Schlafly & DESI Collaboration 2021). To estimate the contamination rate of the crossmatch, we computed the number density of *Euclid* Q1 and DESI EDR in their overlapping area (12.5 deg^2), finding values of 285 111 objects/deg^2 and 9104 objects/deg^2, respectively. Using a blunder or contamination radius of 0.″5, we then computed the blunder probability as the number of expected *Euclid* objects in the blunder area and derived the number of random matches as this blunder probability per the number of DESI objects in the overlapping area. We found 1905 random matches, which we used to derive the contamination fraction as the ratio between this number and that of actual matches. We obtain a contamination fraction of 7.6%, which should be taken as an upper limit as it assumes no correlation whatsoever between the *Euclid* and DESI catalogues (see Sect. 3.1).

2.1. Spectroscopically confirmed galaxy pairs

From the parent sample of 24 922 *Euclid* Q1 sources with a DESI spectroscopic counterpart, we selected galaxy pairs based on a spectroscopic z separation of $\Delta z < 0.005$, a projected physical separation[2] of $d \lesssim 50$ kpc, and a redshift range of $0.01 < z < 1$ to exclude high-z quasars and ensure a visual identification of pairs or merger signatures (e.g. Eróstegui et al. 2025). This yields a sample of 619 galaxy pairs in the EDF-N. Since DESI typically undercounts close galaxy pairs due to fibre collisions, we estimate the missing fraction to be 9–14% (see Appendix A for details).

[2] This upper limit is commonly adopted in dual AGN searches, we note that less conservative works consider up to 100 kpc (see review by, e.g. Pfeifle et al. 2024).

2.2. Active galaxies in Euclid

To identify AGNs in the sample of 619 galaxy pairs (Sect. 2.1), we used optical and near-infrared spectroscopy, mid-infrared colours, X-ray, and radio diagnostics. For this, we crossmatched the parent sample of 619 galaxy pairs with the recent catalogue of 229 779 AGN candidates in the *Euclid* Q1 fields of EC:MZ25, who applied mid-infrared colour diagnostics based on Wide-field Infrared Survey Explorer (WISE) AllWISE photometry, emission-line diagnostics based on DESI spectroscopy, and X-ray diagnostics based on an X-ray counterpart in either the 4XMM-DR14 (Webb et al. 2020) or the *Chandra* Source Catalog Release 2 Series (Evans et al. 2024), identified using the Bayesian algorithm `NWAY` (Salvato et al. 2018; see Euclid Collaboration: Roster et al. 2025 for details)[3]. For the radio diagnostics, we searched for radio counterparts in the Very Large Array Sky Survey (VLASS; Gordon et al. 2021) at 3 GHz and in the LOw-Frequency ARray (LOFAR; van Haarlem et al. 2013) survey of the EDF-N at 144 MHz using the high band antenna (HBA; Bondi et al. 2024). For VLASS we used a commonly adopted search radius of 5″. For LOFAR we used the Bisigello et al. (2025) catalogue, which includes optical-to-near-infrared counterparts for 99.2% of the LOFAR sources presented in the catalogue by Bondi et al. (2024).

We then selected AGNs as those sources satisfying at least one of the following nine criteria:

i A DESI spectral type classification (`SPECTYPE=QSO`, DESI Collaboration et al. 2024).
For sources classified as galaxies (`SPECTYPE=GALAXY`, DESI Collaboration et al. 2024), and using the emission-line fluxes, widths, and equivalent widths provided by `FastSpecFit` (Moustakas et al. 2023):

ii The detection of broad Hα, Hβ, Mg II, or C IV emission lines with a full width at half maximum (FWHM) $\geq 1200\,\mathrm{km\,s^{-1}}$.

iii An AGN classification in either the N II ([O III]λ5007/Hβ vs. [N II]λ6583/Hα), S II ([O III]λ5007/Hβ vs. [S II]λ6717,6731/Hα), or O I ([O III]λ5007/Hβ vs. [O I]λ6300) emission-line diagnostic (BPT) diagrams (Baldwin et al. 1981; Kewley et al. 2001, 2006; Kauffmann et al. 2003; Schawinski et al. 2007; Law et al. 2021), with the composite star-forming (SF)/AGN classification also included for the N II BPT diagram.

iv A strong or weak AGN classification in the WHAN diagram (Cid Fernandes et al. 2010).

v An AGN classification in either the BLUE BPT (Lamareille 2010) or the KEX (Zhang & Hao 2018) diagnostic diagrams, both of which enable AGN identification at $z \gtrsim 0.5$ when the BPT diagrams are not available. For the BLUE BPT diagram, we again considered the composite SF/AGN classification.
All the emission lines used in the emission-line diagnostics were required to have a signal-to-noise ratio of S/N ≥ 3.

vi The detection of broad near-infrared emission lines (FWHM $\geq 1200\,\mathrm{km\,s^{-1}}$), using spectroscopy from *Euclid*'s NISP instrument. Spectra were fitted whenever the S/N of the emission lines was sufficient to ensure a meaningful fit and analysis. We applied a custom interactive fitting procedure designed to simultaneously model each spectrum with a power-law continuum, a set of emission lines, and Fe emission complexes based on Fe templates generated with `Cloudy` (Ferland et al. 1998). The fitting code is based on the Levenberg–Marquardt algorithm implemented in the Python package `Lmfit` (Newville et al. 2016), which allows flexible and robust parameter optimisation (see Appendix D).

vii An AGN classification based on the Assef et al. (2018) 75% completeness and 90% reliability diagnostics, using the *Euclid* WISE AllWISE counterparts (see EC:MZ25 for further details).

viii An X-ray excess at 2–10 keV of at least 3σ above the expected X-ray emission from X-ray binaries (XRBs; e.g. Mezcua et al. 2016, 2018), with the latter computed from the star formation rate and M_* derived from SED fitting (see Sect. 2.3) following Lehmer et al. (2010).

ix A radio excess of at least 3σ above the expected radio emission from stellar processes (e.g. Mezcua et al. 2019; Reines et al. 2020; see Appendix C).

2.3. SED fitting

The stellar masses and star formation rates of the host galaxies were measured via SED fitting. The photometric data were compiled by EC:MZ25 and include *Euclid* photometry (I_E, Y_E, J_E, and H_E), optical fluxes in the *ugriz* bands from the UNIONS surveys (Gwyn et al. 2025), Galaxy Evolution Explorer (GALEX) near- and far-ultraviolet fluxes, and mid-infrared fluxes from WISE bands 1–4 or *Spitzer* IRAC channels 1–2 if WISE was not available. The redshifts come from DESI EDR spectroscopy (see EC:MZ25 for more details). To account for AGN emission in the SED fitting, we used the well-established and computationally efficient SED fitting `Code Investigating GALaxy Emission` (`CIGALE`; Boquien et al. 2019; Yang et al. 2022), adopting a delayed star formation history with exponential decrease in combination with the physically motivated AGN model `SKIRTOR` (Stalevski et al. 2016). Further details on the SED fitting method and setup are available in Euclid Collaboration: Laloux et al. (2026), who developed a method to quantify the reliability of such SED-derived properties as stellar mass by using mock SEDs built from observed quasars and galaxies. In particular, the stellar mass reliability, $R_{M_\star}$, corresponds to the probability of the difference with the true value being smaller than both 0.5 dex and the measured uncertainties. Euclid Collaboration: Laloux et al. (2026) also provide a multiplicative factor to obtain larger and more realistic uncertainties to reach at least 0.68 reliability (1σ). These updated uncertainties are incorporated in Table 1. Based on the available photometry, SED fitting can be performed for 24 790 out of the 24 922 *Euclid* Q1 sources with a DESI spectroscopic counterpart. Applying a stellar mass cut $\log_{10}(M_*/M_\odot) \leq 10$ to select low-mass galaxies results in 11 863 low-mass galaxies and 12 927 massive galaxies. To further ensure the robustness of the stellar masses of the dual AGN host galaxies, we used the χ^2 and the $R_{M_\star}$ parameters derived in Euclid Collaboration: Laloux et al. (2026) and identified as high-confidence fits those sources with reduced $\chi^2 \leq 10$ and $R_{M_\star} > 0.5$. This reduced χ^2 threshold has been empirically established to eliminate SED fits with spurious or uncertain photometry (Euclid Collaboration: Laloux et al. 2026). Two examples of the SED fitting performed by `CIGALE` are shown in Fig. B.

3. Results and discussion

3.1. Spectroscopically confirmed dual AGNs

In 58 out of the 619 galaxy pairs, each of the two galaxies is found to host an AGN based on at least one of the selection criteria described in Sect. 2.2, thus yielding a sample of 58 dual

[3] The eROSITA first Data Release (Merloni et al. 2024) does not cover EDF-N.

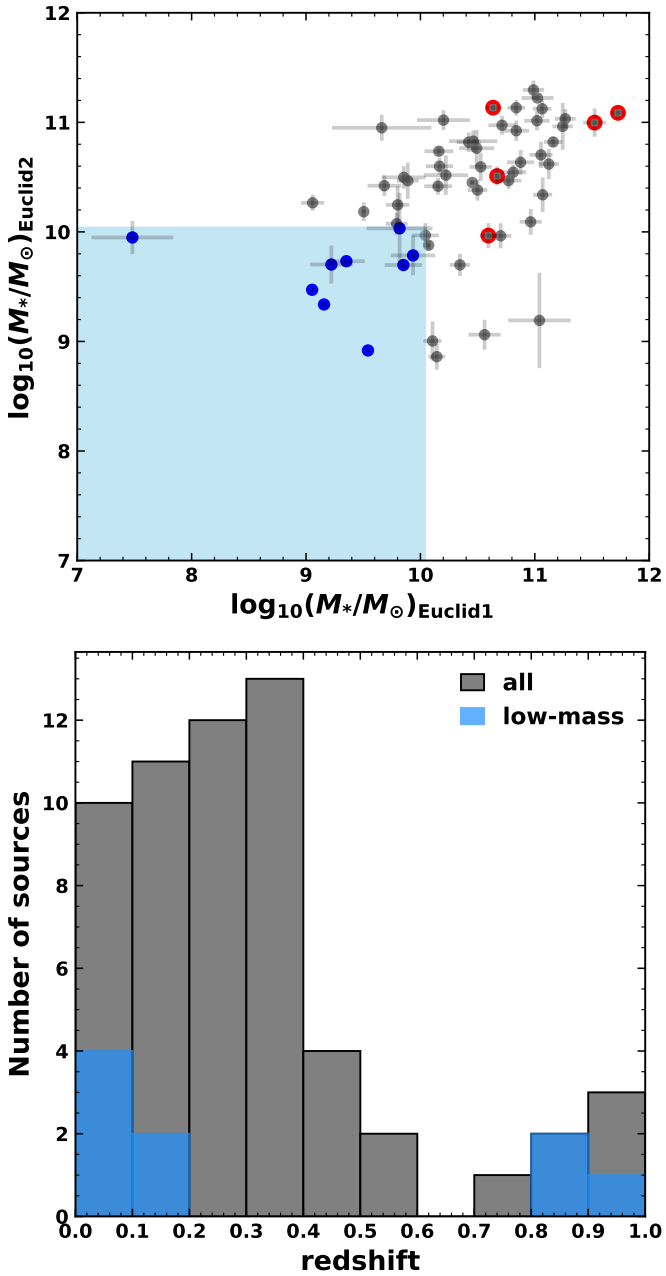

Fig. 1. *Top*: Stellar mass for each of the two galaxies (Euclid1 and Euclid2, with indexes 1 and 2 randomly assigned) for the 58 dual AGN candidates. The blue area shows the low-mass regime [$\log_{10}(M_*/M_\odot) \leq 10$] used to select dual AGNs in low-mass galaxies (blue dots). All the sources have high-confidence stellar masses based on SED fitting (with $\chi^2 \leq 10$ and $R_{M_\star} > 0.5$; see text) except for the five sources marked in red ($R_{M_\star} < 0.5$). *Bottom*: Spectroscopic redshift distribution of the 58 dual AGNs (grey bars) and the nine dual AGNs in low-mass galaxies (blue bars).

AGN candidates (Fig. 1, top). All the dual AGN systems have SED fits with reduced $\chi^2 \leq 10$ and $R_{M_\star} > 0.5$ except for five systems (marked in red in Fig. 1) with $R_{M_\star} < 0.5$. The spectroscopic redshifts for this sample of 58 dual AGNs range from $z = 0.027$ to 0.950 (Fig. 1, bottom), with a gap at $z \sim 0.6$ due to the sources being either DESI Bright Galaxy Survey (whose distribution peaks at $z \sim 0.2$) or Emission Line Galaxy (peak at $z \sim 1.0$) targets (see Fig. 2 in DESI Collaboration et al. 2024). The projected separation, $D_{\rm proj}$, between the two AGNs ranges from $D_{\rm proj} = 11.2$ kpc to 51.8 kpc (Fig. 2). In twelve of these systems, the two AGNs are identified by at least two diagnostics and can thus be considered 'robust' dual AGNs. The remaining 46 systems, in which one or both AGNs are identified based on only one diagnostic, can be conservatively considered as 'candidate' dual AGNs.

We recomputed the contamination fraction of the *Euclid* Q1 and DESI EDR crossmatch adopting a VIS limiting magnitude for *Euclid* Q1 of 24.3 mag, which corresponds to the faintest DESI r-band magnitude of the AGN candidates in the dual AGN sample. This yields a *Euclid* number density in the overlapping area between *Euclid* Q1 and DESI EDR of 70 542 objects/deg^2 and a contamination fraction of 1.9%, which implies that one out of the 58 dual AGN systems could be a mismatch. Yet, an individual visual inspection of the *Euclid* VIS images and their DESI spectroscopic counterparts confirms they are systems within the 0.″5 radius used in the *Euclid* Q1 and DESI EDR crossmatch.

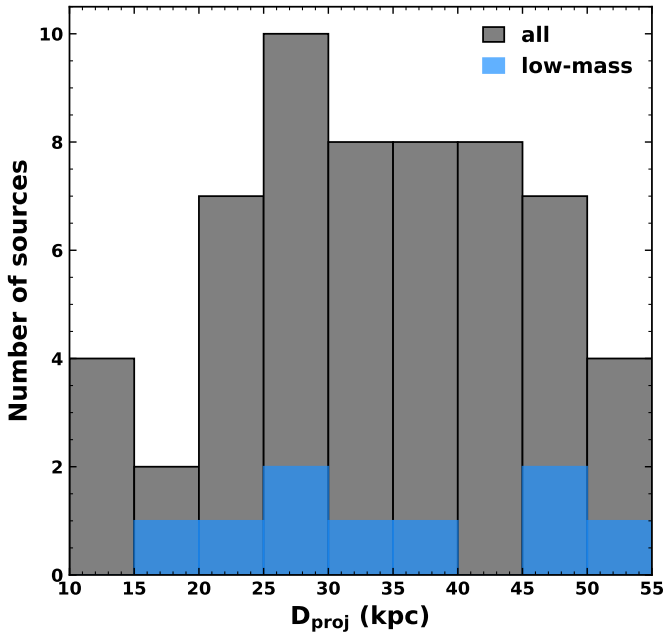

Fig. 2. Projected distance distribution of the 58 dual AGN candidates (grey bars) and the nine dual AGNs in low-mass galaxies (blue bars).

3.2. Dual AGNs in low-mass galaxies

Nine of the 58 dual AGN candidates have $\log_{10}(M_*/M_\odot) \leq 10$, yielding a final sample of nine dual AGNs in low-mass galaxies (see Fig. 3). All of the 18 AGN host galaxies have SED fits with reduced $\chi^2 \leq 7$ and $R_{M_\star} > 0.5$. Of these, 17 have $R_{M_\star} \geq 0.8$, and 14 have reduced $\chi^2 < 3$. Three of the dual AGN systems are located at $z \simeq 0.9$ and are identified as AGNs by the BLUE and KEX diagrams. The remaining six systems are at $z \lesssim 0.1$ and are classified as AGNs based on optical, infrared, or radio (LOFAR) diagnostics (Table 1 reports the criteria for each source). Of the nine dual AGNs in low-mass galaxies, one can be considered 'robust' because of the two AGNs classified as such by two diagnostics (see Table 1). The remaining systems are considered 'candidates', since they are classified as AGNs by only one diagnostic. The latter is particularly relevant for those sources close to the SF/AGN demarcation lines in the BLUE, KEX, or [S II]-BPT diagrams, such as EUCL J175306.12+645855.3, whose po-

sition in the [S II]-BPT is nearly at the intersection between the SF and the AGN region (see Appendix E).

3.2.1. Radio counterparts and lack of X-ray detections

None of the 18 sources in the sample of nine dual AGN candidates in low-mass galaxies have a VLASS counterpart. Eight have a radio counterpart in the LOFAR coverage of the EDF-N with the HBA (Bondi et al. 2024), consistent with an AGN origin. The LOFAR–*Euclid* associations – while performed using robust maximum likelihood techniques and vetted catalogues (see Appendix C) – may be particularly challenging in the low-stellar-mass regime. In Appendix C, we estimate a LOFAR contamination fraction of 8.3% based on random match statistics; however, this likely represents a lower limit as the reliability of radio associations degrades at low stellar masses due to weaker radio fluxes and higher source densities (e.g. Kondapally et al. 2021; *Euclid* Collaboration: Visser et al. in prep). Using a Monte Carlo analysis, *Euclid* Collaboration: Visser et al. (in prep) find that the average contamination fraction is $\sim$ 20% in the stellar mass range $9.0 \leq \log_{10}(M_*/M_\odot) \leq 10.0$.

None of the dual AGNs in low-mass galaxies are found to have X-ray detections in the *Chandra* Source Catalog (they are outside of its footprint) or in 4XMM-DR14. Upper limits (at a 3σ significance) on the 0.2–12 keV fluxes can be obtained from XMM Slew and pointed observations[4] for all the AGNs in the dual AGN low-mass systems. Assuming a power-law photon index $\Gamma = 2$, we find upper limits on the 0.2–12 keV X-ray luminosities ranging from 10^{42} erg s^{-1} to 10^{47} erg s^{-1}, higher than those typically found in X-ray-emitting AGNs in local low-mass galaxies ($< 10^{42}$ erg s^{-1}; e.g. Schramm et al. 2013; Baldassare et al. 2017; Eberhard & Reines 2025).

3.2.2. Black hole masses

We derived the black hole masses of the dual AGNs in low-mass galaxies using the M_*–$M_{\rm BH}$ correlation of Pucha et al. (2025) for confident broad-line AGN candidates (their Equation 3). We find that the black holes masses are in the range $\log_{10}(M_{\rm BH}/M_\odot) = 4.0$–$6.7$ with a typical uncertainty of 0.5 dex (see Table 2).

One of the sources (EUCL J174727.18+662623.6) presents broad H α emission (see Appendix E), from which Pucha et al. (2025) derive a black hole mass of $\log_{10}(M_{\rm BH}/M_\odot) = 7.7 \pm 0.5$ using single-epoch virial techniques. For this source we also fitted the *Euclid* NISP spectrum (see Fig. D.1), in particular the Paβ and He I emission lines. Both have a FWHM ≥ 1200 km s^{-1}, indicative of a broad-line region origin. Using the Paβ relation (see Appendix D) from La Franca et al. (2015) accounting for the same virial factor ($\epsilon = 1$) as Pucha et al. (2025), we obtain a black hole mass of $\log_{10}(M_{\rm BH}/M_\odot) = 7.8 \pm 0.5$, fully consistent with that derived from the broad H α emission. For the He I, we used the relations from Ricci et al. (2017, 2022) and obtain a black hole mass of $\log_{10}(M_{\rm BH}/M_\odot) = 7.9 \pm 0.5$ (see eq. D.4 in Appendix D).

We note that for EUCL J174727.18+662623.6 the black hole mass inferred from the DESI and *Euclid* spectra is only marginally consistent with that derived from the M_*–$M_{\rm BH}$ calibration of Pucha et al. (2025) within its quoted scatter. This illustrates that individual systems may deviate significantly from simple black hole-galaxy scaling relations and that direct spectroscopic estimates can be important to estimate such masses.

[4] https://xmmuls.esac.esa.int/upperlimitserver/

3.2.3. Merger stage

The $D_{\rm proj}$ values between the two AGN candidates in the sample of nine dual AGNs in low-mass galaxies range from 19.5 kpc to 50.9 kpc, which suggests they are all either in an early merger stage or have undergone at least a first pass (e.g. Eróstegui et al. 2025). A visual inspection of the VIS images indeed reveals tidal signatures in some of the sources (e.g. EUCL J175226.38+662659.0 and EUCL J174727.18+662623.6 in Fig. 3), while most of the systems seem to be close pairs of galaxies yet to undergo a merger process. This supports previous findings suggesting that AGNs in dwarf galaxies are not necessarily activated by merger events (Eróstegui et al. 2025).

3.2.4. Dual AGN fraction

The sample of nine dual AGNs in low-mass galaxies reported in this paper allows us to derive for the first time a dual AGN fraction in low-mass galaxies. Because of incompleteness effects (the dual AGN candidate sample is based on different surveys and thus different target samples), the fraction should be taken as a lower limit. We define the dual AGN fraction as the ratio of the dual AGN systems to the total number of low-mass galaxies in the sample (9/11 863), finding a 0.1% dual AGN fraction for low-mass galaxies. In the case of massive galaxies, the dual AGN fraction is found to be 0.4% (49/12 927). The lower dual AGN fraction for low-mass galaxies is expected given the decline of black hole occupation fraction and of AGN fraction with stellar mass found observationally (e.g. Miller et al. 2015; Mezcua et al. 2018; Birchall et al. 2020; Bykov et al. 2024; Zou et al. 2025) and in simulations (e.g. Bellovary et al. 2019; Pacucci et al. 2021).

Although the dual AGN fractions here derived should be taken with caution, they are at least an order of magnitude smaller than those observed in nearby massive systems (e.g. 7.8% for ultra-hard X-ray-selected AGNs – Koss et al. 2012 – and 1.3% based on optical emission-line diagnostics – Liu et al. 2011, both at separations ≤ 30 kpc), even when considering the total dual AGN fraction of 0.2%, which accounts for both low-mass and massive galaxies. Yet, this dual AGN fraction seems consistent with that expected from large-scale hydrodynamical simulations in which the dual AGN fraction (including both low-mass and massive galaxies) is 0.1% at $z \leq 0.5$ (Rosas-Guevara et al. 2019; Volonteri et al. 2022; Puerto-Sánchez et al. 2025). The dual AGN fraction derived here is also consistent with that from models in which AGN activity is triggered in gas-rich progenitor galaxies when the nuclei of these galaxies are roughly within the half-light radii of their companion galaxies (Yu et al. 2011).

3.2.5. Progenitors of future gravitational wave LISA sources

To assess the potential relevance of the dual AGNs in low-mass galaxies for future gravitational wave detections as the black holes approach coalescence, we estimated the merger timescales $t_{\rm c}$ from the prescription of Kitzbichler & White (2008):

$$t_{\rm c} = 2.2\,{\rm Gyr}\,\frac{D_{\rm proj}}{50\,{\rm kpc}}\left(\frac{M_\star}{4\times10^{10}\,h^{-1}\,M_\odot}\right)^{-0.3}\left(1+\frac{z}{8}\right), \quad (1)$$

where $M_\star$ is the major stellar mass of the galaxies in the system and $h = 0.7$. This results in $t_{\rm c} = 1.9$–5.2 Gyr. The black hole masses derived in Sect. 3.2.2 imply observed innermost sta-

Table 1. Sample of nine dual AGN candidates in low-mass galaxies.

Euclid1	Euclid2	z_1	z_2	$D_{\rm proj}$ [kpc]	$\log_{10}(M_*/M_\odot)_1$	$\log_{10}(M_*/M_\odot)_2$
EUCL J175226.38+662659.0 radio	EUCL J175228.85+662646.8 radio	0.052	0.052	19.5	9.16 ± 0.02	9.34 ± 0.02
EUCL J180150.12+670229.9 N II-BPT, BLUE, radio	EUCL J180154.58+670240.4 radio	0.087	0.088	46.1	9.05 ± 0.02	9.47 ± 0.02
EUCL J181025.14+664252.8 radio	EUCL J181026.79+664235.5 radio	0.088	0.088	32.7	9.54 ± 0.02	8.92 ± 0.02
EUCL J180219.39+664532.8 WHAN	EUCL J180221.60+664521.3 WHAN	0.089	0.088	28.8	9.4 ± 0.2	9.73 ± 0.02
EUCL J175306.12+645855.3 S II-BPT	EUCL J175305.12+645839.0 WHAN	0.119	0.118	37.5	7.5 ± 1.3	9.9 ± 0.2
EUCL J174727.18+662623.6 N II-BPT, S II-BPT, broad H α, broad Pa β, BLUE, KEX, WISE, radio	EUCL J174726.73+662605.0 radio	0.142	0.142	47.1	9.9 ± 0.2	9.70 ± 0.06
EUCL J175759.76+654524.6 BLUE, KEX	EUCL J175759.89+654521.9 BLUE, KEX	0.876	0.875	21.2	9.9 ± 0.2	9.8 ± 0.2
EUCL J175256.05+653844.8 KEX	EUCL J175257.08+653846.1 BLUE, KEX	0.893	0.894	50.9	9.2 ± 0.3	9.7 ± 0.2
EUCL J174816.82+632750.0 KEX	EUCL J174817.34+632751.2 BLUE, KEX	0.933	0.931	29.0	9.8 ± 0.5	10.0 ± 0.5

Notes. The second row under each *Euclid* ID indicates the diagnostic that classifies the source as an AGN. The labels Euclid1 and Euclid2 are randomly assigned.

Table 2. Black hole masses of the dual AGNs in low-mass galaxies derived using the M_*–$M_{\rm BH}$ correlation of Pucha et al. (2025).

Euclid1	Euclid2	$\log_{10}(M_{\rm BH}/M_\odot)_1$	$\log_{10}(M_{\rm BH}/M_\odot)_2$
EUCL J175226.38+662659.0	EUCL J175228.85+662646.8	5.7 ± 0.4	5.9 ± 0.4
EUCL J180150.12+670229.9	EUCL J180154.58+670240.4	5.6 ± 0.4	6.1 ± 0.4
EUCL J181025.14+664252.8	EUCL J181026.79+664235.5	6.1 ± 0.4	5.5 ± 0.4
EUCL J180219.39+664532.8	EUCL J180221.60+664521.3	5.9 ± 0.6	6.3 ± 0.5
EUCL J175306.12+645855.3	EUCL J175305.12+645839.0	4.0 ± 1.7	6.6 ± 0.6
EUCL J174727.18+662623.6	EUCL J174726.73+662605.0	7.8 ± 0.5†	6.3 ± 0.5
EUCL J175759.76+654524.6	EUCL J175759.89+654521.9	6.6 ± 0.6	6.4 ± 0.6
EUCL J175256.05+653844.8	EUCL J175257.08+653846.1	5.8 ± 0.7	6.3 ± 0.6
EUCL J174816.82+632750.0	EUCL J174817.34+632751.2	6.4 ± 0.9	6.7 ± 0.9

Notes. † Black hole mass derived from the broad Pa β line.

ble circular orbit frequencies $f_{\rm ISCO}$ in the interval $\sim$ 0.5–5 mHz, where

$$f_{\rm ISCO} = \frac{c^3}{2\pi G M_{\rm BH}} \frac{1}{6^{3/2}}\,, \tag{2}$$

and G is the gravitational constant.

Under standard assumptions for the LISA sensitivity curve (LISA Definition Study Report; Colpi et al. 2024) and assuming that these pairs evolve into bound black hole binaries and coalesce, their late-inspiral gravitational wave emission could, in principle, be detectable by LISA. We stress, however, that the estimated merger timescales are in some cases longer than the look-back time at the observed redshift, implying that coalescence may occur only at later cosmic times and that AGN activity will not likely remain continuously strong throughout the full merger sequence.

A full reassessment of the space density of such systems and of the corresponding LISA event rate, incorporating these revised black hole masses, merger timescales, and stellar mass functions, is beyond the scope of this work and will be addressed elsewhere. In particular, the relative fraction of low-mass hosts in our sample compared to more massive galaxies should be regarded as a strict lower limit: incompleteness and selection biases, especially against faint and intermediate- to high-redshift systems, almost certainly suppress the observed incidence of such low-mass pairs. Consequently, the contribution of the black hole binaries that may eventually descend from these systems to the overall rate of LISA-detectable coalescences will depend sensitively on a careful treatment of incompleteness and selection effects.

4. Conclusions

In this paper we reported the first sample of nine dual AGNs in low-mass galaxies to date, along with a new sample of 49 dual AGNs in massive galaxies, using *Euclid* photometry and spec-

troscopy, DESI spectroscopy, mid-infrared colours, and LOFAR radio counterparts. The redshifts of the nine dual AGNs in low-mass galaxies range from ∼ 0.05 to 0.9, and the AGN-projected separations range from 19.5 to 50.9 kpc. We derive a 0.1% dual AGN fraction in low-mass galaxies and estimate that these systems likely trace a population of progenitor black-hole pairs that may evolve into bound binaries and eventually coalesce, emitting gravitational waves in the LISA band.

The finding that dual AGNs can form in low-mass galaxies has important implications for seed black hole models, since it provides an avenue for black hole growth if the two black holes coalesce (Tamfal et al. 2018). Thus, these black holes in local dwarf galaxies might not be the unevolved relics of the early-Universe seed black holes (Mezcua 2019). The systems identified here can be regarded as possible progenitors of future LISA sources, reinforcing the importance of including dwarf galaxy mergers and dual AGNs in dwarf galaxies in predictions of binary black hole mergers and the gravitational wave background (Saeedzadeh et al. 2024). Their contribution to the rate of LISA-detectable black-hole mergers will, however, depend on the time delay between the dual AGN phase and black-hole coalescence, as well as on AGN activity and selection effects.

Acknowledgements. The Euclid Consortium acknowledges the European Space Agency and a number of agencies and institutes that have supported the development of *Euclid*, in particular the Agenzia Spaziale Italiana, the Austrian Forschungsförderungsgesellschaft funded through BMIMI, the Belgian Science Policy, the Canadian Euclid Consortium, the Deutsches Zentrum für Luft- und Raumfahrt, the DTU Space and the Niels Bohr Institute in Denmark, the French Centre National d'Etudes Spatiales, the Fundação para a Ciência e a Tecnologia, the Hungarian Academy of Sciences, the Ministerio de Ciencia, Innovación y Universidades, the National Aeronautics and Space Administration, the National Astronomical Observatory of Japan, the Netherlandse Onderzoekschool Voor Astronomie, the Norwegian Space Agency, the Research Council of Finland, the Romanian Space Agency, the Swiss Space Office (SSO) at the State Secretariat for Education, Research, and Innovation (SERI), and the United Kingdom Space Agency. A complete and detailed list is available on the *Euclid* web site (www.euclid-ec.org/consortium/community/). This work has made use of the *Euclid* Quick Release Q1 data from the *Euclid* mission of the European Space Agency (ESA), 2025, https://doi.org/10.57780/esa-2853f3b. LOFAR data products were provided by the LOFAR Surveys Key Science project (LSKSP; https://lofar-surveys.org/) and were derived from observations with the International LOFAR Telescope (ILT). LOFAR (van Haarlem et al. 2013) is the Low Frequency Array designed and constructed by ASTRON. It has observing, data processing, and data storage facilities in several countries, which are owned by various parties (each with their own funding sources), and which are collectively operated by the ILT foundation under a joint scientific policy. The efforts of the LSKSP have benefited from funding from the European Research Council, NOVA, NWO, CNRS-INSU, the SURF Co-operative, the UK Science and Technology Funding Council and the Jülich Supercomputing Centre. M.M. acknowledges support from the Spanish Ministry of Science and Innovation through the project PID2021-124243NBC22. This work was partially supported by the program Unidad de Excelencia María de Maeztu CEX2020-001058-M. B.L., J.C., and F.R. acknowledge the support from the INAF Large Grant "AGN & *Euclid*: a close entanglement" Ob. Fu. 01.05.23.01.14. A.F. acknowledges the support from project "VLT- MOONS" CRAM 1.05.03.07, INAF Large Grant 2022 "Dual and binary SMBH in the multi-messenger era" Ob. Fu. 1.05.12.01.13, and INAF Mini Grant 2024 "The pc-scale view of HII regions in M33" Ob. Fu. 1.05.24.07.01. ELSA: Euclid Legacy Science Advanced analysis tools" (Grant Agreement no. 101135203) is funded by the European Union. Views and opinions expressed are however those of the author(s) only and do not necessarily reflect those of the European Union or Innovate UK. Neither the European Union nor the granting authority can be held responsible for them. UK participation is funded through the UK Horizon guarantee scheme under Innovate UK grant 10093177. The authors acknowledge the use of computational resources from the parallel computing cluster of the Open Physics Hub (https://site.unibo.it/openphysicshub/en) at the Physics and Astronomy Department in Bologna.

References

Alexander, D. M., Hickox, R. C., Aird, J., et al. 2025, New A Rev., 101, 101733
Assef, R. J., Stern, D., Noirot, G., et al. 2018, ApJS, 234, 23
Baldassare, V. F., Reines, A. E., Gallo, E., & Greene, J. E. 2017, ApJ, 836, 20
Baldwin, J. A., Phillips, M. M., & Terlevich, R. 1981, PASP, 93, 5
Bellovary, J. M., Cleary, C. E., Munshi, F., et al. 2019, MNRAS, 482, 2913
Bianchi, D., Hanif, M., Carnero Rosell, A., et al. 2025, JCAP, 4, 50
Bichang'a, B., Kaviraj, S., Lazar, I., et al. 2024, MNRAS, 532, 613
Birchall, K. L., Watson, M. G., & Aird, J. 2020, MNRAS, 492, 2268
Bisigello, L., Giulietti, M., Prandoni, I., et al. 2025, The Open Journal of Astrophysics, 8
Bogdán, Á., Goulding, A. D., Natarajan, P., et al. 2024, Nature Astronomy, 8, 126
Bondi, M., Scaramella, R., Zamorani, G., et al. 2024, A&A, 683, A179
Boquien, M., Burgarella, D., Roehlly, Y., et al. 2019, A&A, 622, A103
Bykov, S. D., Gilfanov, M. R., & Sunyaev, R. A. 2024, MNRAS, 527, 1962
Cid Fernandes, R., Stasińska, G., Schlickmann, M. S., et al. 2010, MNRAS, 403, 1036
Ciurlo, A., Mannucci, F., Yeh, S., et al. 2023, A&A, 671, L4
Colpi, M., Danzmann, K., Hewitson, M., et al. 2024, arXiv:2402.07571
De Rosa, A., Vignali, C., Bogdanović, T., et al. 2019, New A Rev., 86, 101525
De Rosa, A., Vignali, C., Severgnini, P., et al. 2023, MNRAS, 519, 5149
de Ruiter, H. R., Willis, A. G., & Arp, H. C. 1977, A&AS, 28, 211
Deason, A., Wetzel, A., & Garrison-Kimmel, S. 2014, ApJ, 794, 115
DESI Collaboration, Adame, A. G., Aguilar, J., et al. 2024, AJ, 168, 58
Eberhard, J.-M. & Reines, A. E. 2025, ApJ, 994, 1
Eróstegui, A., Mezcua, M., Siudek, M., Domínguez Sánchez, H., & Rodríguez Morales, V. 2025, A&A, 699, A330
Euclid Collaboration: Aussel, H., Tereno, I., Schirmer, M., et al. 2025, A&A, in press, arXiv:2503.15302
Euclid Collaboration: Cropper, M., Al-Bahlawan, A., Amiaux, J., et al. 2025, A&A, 697, A2
Euclid Collaboration: Fabricius, M. et al. 2026, A&A, in press, arXiv:2503.15313
Euclid Collaboration: Jahnke, K., Gillard, W., Schirmer, M., et al. 2025, A&A, 697, A3
Euclid Collaboration: Laloux, B. et al. 2026, A&A, submitted
Euclid Collaboration: Matamoro Zatarain, T., Fotopoulou, S., Ricci, F., et al. 2025, A&A, in press (Euclid Q1 SI), https://doi.org/10.1051/0004-6361/202554619, arXiv:2503.15320
Euclid Collaboration: Mellier, Y., Abdurro'uf, Acevedo Barroso, J., et al. 2025, A&A, 697, A1
Euclid Collaboration: Roster, W., Salvato, M., Buchner, J., et al. 2025, A&A, in press (Euclid Q1 SI), https://doi.org/10.1051/0004-6361/202554616, arXiv:2503.15316
Euclid Collaboration: Scaramella, R., Amiaux, J., Mellier, Y., et al. 2022, A&A, 662, A112
Euclid Collaboration: Schirmer, M., Jahnke, K., Seidel, G., et al. 2022, A&A, 662, A92
Euclid Quick Release Q1. 2025, https://doi.org/10.57780/esa-2853f3b
Evans, I. N., Evans, J. D., Martínez-Galarza, J. R., et al. 2024, ApJS, 274, 22
Ferland, G. J., Korista, K. T., Verner, D. A., et al. 1998, PASP, 110, 761
Flores, I., Mezcua, M., & Rodríguez Morales, V. 2025, A&A, 704, A267
Gordon, Y. A., Boyce, M. M., O'Dea, C. P., et al. 2021, ApJS, 255, 30
Greene, J. E., Strader, J., & Ho, L. C. 2020, ARA&A, 58, 257
Gwyn, S., McConnachie, A. W., Cuillandre, J.-C., et al. 2025, AJ, 170, 324
Hopkins, P. F., Hernquist, L., Cox, T. J., et al. 2006, ApJS, 163, 1
Kauffmann, G., Heckman, T. M., Tremonti, C., et al. 2003, MNRAS, 346, 1055
Kaviraj, S., Martin, G., & Silk, J. 2019, MNRAS, 489, L12
Kewley, L. J., Dopita, M. A., Sutherland, R. S., Heisler, C. A., & Trevena, J. 2001, ApJ, 556, 121
Kewley, L. J., Groves, B., Kauffmann, G., & Heckman, T. 2006, MNRAS, 372, 961
Kitzbichler, M. G. & White, S. D. M. 2008, MNRAS, 391, 1489
Komossa, S., Burwitz, V., Hasinger, G., et al. 2003, ApJ, 582, L15
Kondapally, R., Best, P. N., Hardcastle, M. J., et al. 2021, A&A, 648, A3
Koss, M., Mushotzky, R., Treister, E., et al. 2012, ApJ, 746, L22
Koss, M. J., Treister, E., Kakkad, D., et al. 2023, ApJ, 942, L24
La Franca, F., Onori, F., Ricci, F., et al. 2015, MNRAS, 449, 1526
Lamareille, F. 2010, A&A, 509, A53
Lamperti, I., Koss, M., Trakhtenbrot, B., et al. 2017, MNRAS, 467, 540
Law, D. R., Ji, X., Belfiore, F., et al. 2021, ApJ, 915, 35
Lehmer, B. D., Alexander, D. M., Bauer, F. E., et al. 2010, ApJ, 724, 559
Liu, X., Shen, Y., Strauss, M. A., & Hao, L. 2011, ApJ, 737, 101
Maiolino, R., Scholtz, J., Witstok, J., et al. 2024, Nature, 627, 59
Mannucci, F., Pancino, E., Belfiore, F., et al. 2022, Nature Astronomy, 6, 1185
Mannucci, F., Scialpi, M., Ciurlo, A., et al. 2023, A&A, 680, A53
Manzano-King, C. M. & Canalizo, G. 2020, MNRAS, 498, 4562
Merloni, A., Lamer, G., Liu, T., et al. 2024, A&A, 682, A34
Mezcua, M. 2017, International Journal of Modern Physics D, 26, 1730021
Mezcua, M. 2019, Nature Astronomy, 3, 6

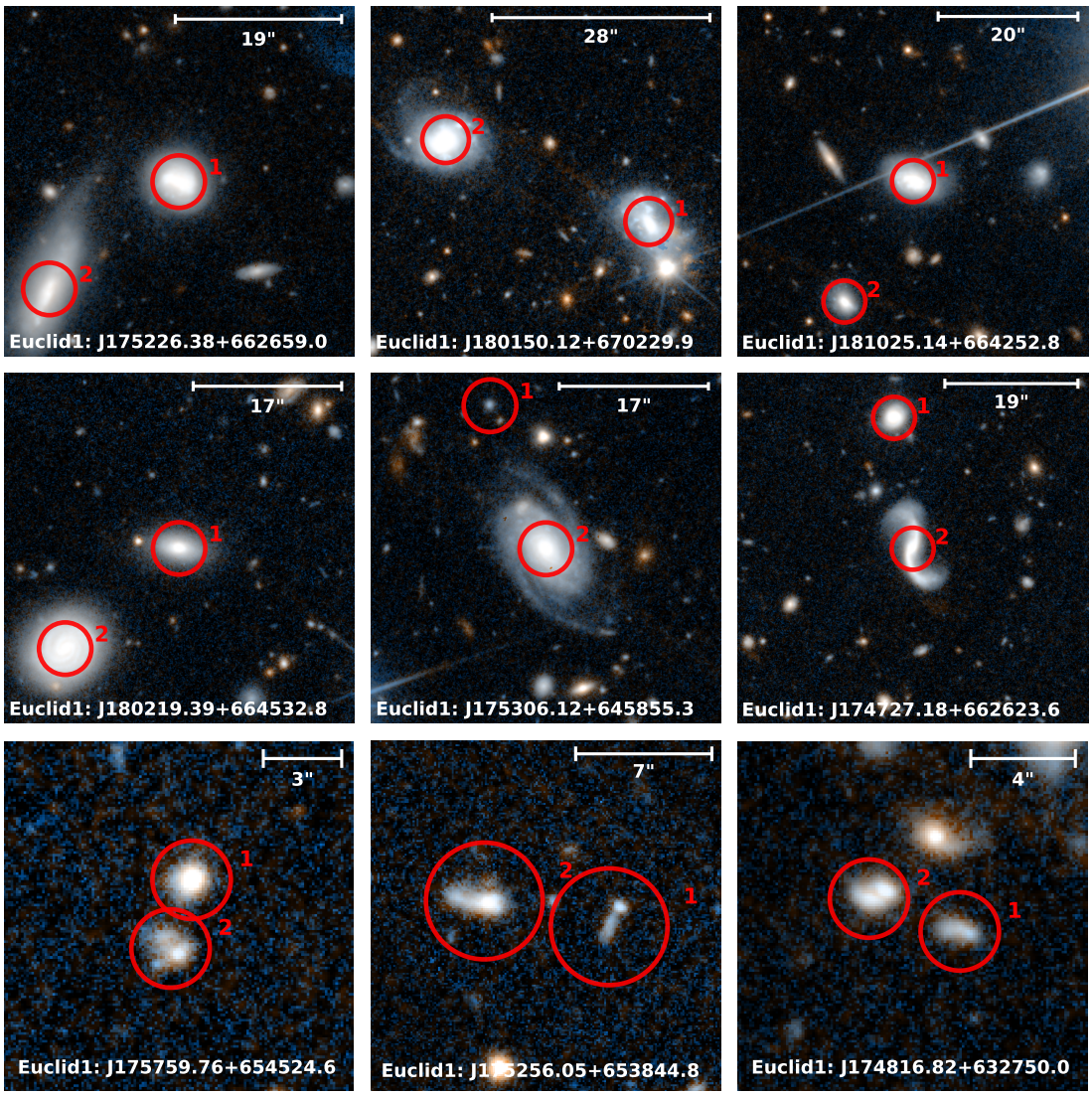

Fig. 3. Composite VIS- and NISP-band images of the nine dual AGN candidates in low-mass galaxies sorted in ascending redshift, as in Table 1. The red circles mark the positions of the AGNs. The scale bars show the separation between the two candidate AGNs in arcsec.

Mezcua, M., Civano, F., Fabbiano, G., Miyaji, T., & Marchesi, S. 2016, ApJ, 817, 20
Mezcua, M., Civano, F., Marchesi, S., et al. 2018, MNRAS, 478, 2576
Mezcua, M. & Domínguez Sánchez, H. 2020, ApJ, 898, L30
Mezcua, M. & Domínguez Sánchez, H. 2024, MNRAS, 528, 5252
Mezcua, M., Pacucci, F., Suh, H., Siudek, M., & Natarajan, P. 2024, ApJ, 966, L30
Mezcua, M., Siudek, M., Suh, H., et al. 2023, ApJ, 943, L5
Mezcua, M., Suh, H., & Civano, F. 2019, MNRAS, 488, 685
Mićić, M., Irwin, J. A., Nair, P., et al. 2024, ApJ, 968, L21
Miller, B. P., Gallo, E., Greene, J. E., et al. 2015, ApJ, 799, 98
Mohan, N. & Rafferty, D. 2015, PyBDSF: Python Blob Detection and Source Finder, Astrophysics Source Code Library, record ascl:1502.007
Moustakas, J., Scholte, D., Dey, B., & Khederlarian, A. 2023, FastSpecFit: Fast spectral synthesis and emission-line fitting of DESI spectra, ASCL, record ascl:2308.005
Newville, M., Stensitzki, T., Allen, D. B., et al. 2016, Lmfit: Non-Linear Least-Square Minimization and Curve-Fitting for Python, Astrophysics Source Code Library, record ascl:1606.014
Nisbet, D. M. 2018, PhD thesis, University of Edinburgh, UK
Pacucci, F., Mezcua, M., & Regan, J. A. 2021, ApJ, 920, 134
Paudel, S., Smith, R., Yoon, S. J., Calderón-Castillo, P., & Duc, P.-A. 2018, ApJS, 237, 36
Perna, M., Arribas, S., Lamperti, I., et al. 2025, A&A, 696, A59
Pfeifle, R. W., Weaver, K. A., Secrest, N. J., Rothberg, B., & Patton, D. R. 2024, arXiv:2411.12799
Pinon, M., de Mattia, A., McDonald, P., et al. 2025, JCAP, 1, 41
Pucha, R., Juneau, S., Dey, A., et al. 2025, ApJ, 982, 10
Puerto-Sánchez, C., Habouzit, M., Volonteri, M., et al. 2025, MNRAS, 536, 3016
Reines, A. E. 2022, Nature Astronomy, 6, 26
Reines, A. E., Condon, J. J., Darling, J., & Greene, J. E. 2020, ApJ, 888, 36
Reines, A. E., Greene, J. E., & Geha, M. 2013, ApJ, 775, 116
Ricci, F., La Franca, F., Onori, F., & Bianchi, S. 2017, A&A, 598, A51
Ricci, F., Treister, E., Bauer, F. E., et al. 2022, ApJS, 261, 8
Rosas-Guevara, Y. M., Bower, R. G., McAlpine, S., Bonoli, S., & Tissera, P. B. 2019, MNRAS, 483, 2712
Saeedzadeh, V., Babul, A., Mukherjee, S., et al. 2024, ApJ, 975, 265
Salehirad, S., Reines, A. E., & Molina, M. 2022, ApJ, 937, 7
Salvato, M., Buchner, J., Budavári, T., et al. 2018, MNRAS, 473, 4937
Schawinski, K., Thomas, D., Sarzi, M., et al. 2007, MNRAS, 382, 1415
Schlafly, E. & DESI Collaboration. 2021, in APS Meeting Abstracts, Vol. 2021, APS April Meeting Abstracts, Z08.006
Schramm, M., Silverman, J. D., Greene, J. E., et al. 2013, ApJ, 773, 150
Scialpi, M., Mannucci, F., Marconcini, C., et al. 2024, A&A, 690, A57
Siudek, M., Mezcua, M., & Krywult, J. 2023, MNRAS, 518, 724
Stalevski, M., Ricci, C., Ueda, Y., et al. 2016, MNRAS, 458, 2288
Sutherland, W. & Saunders, W. 1992, MNRAS, 259, 413
Tamfal, T., Capelo, P. R., Kazantzidis, S., et al. 2018, ApJ, 864, L19
Ulivi, L., Mannucci, F., Scialpi, M., et al. 2025, A&A, submitted, arXiv:2508.19494
van Haarlem, M. P., Wise, M. W., Gunst, A. W., et al. 2013, A&A, 556, A2
Volonteri, M. 2010, A&A Rev., 18, 279
Volonteri, M., Pfister, H., Beckmann, R., et al. 2022, MNRAS, 514, 640
Webb, N. A., Coriat, M., Traulsen, I., et al. 2020, A&A, 641, A136

Wild, V., Kauffmann, G., Heckman, T., et al. 2007, MNRAS, 381, 543
Yang, G., Boquien, M., Brandt, W. N., et al. 2022, ApJ, 927, 192
Yu, Q., Lu, Y., Mohayaee, R., & Colin, J. 2011, ApJ, 738, 92
Zhang, K. & Hao, L. 2018, ApJ, 856, 171
Zou, F., Gallo, E., Seth, A. C., et al. 2025, ApJ, 992, 176

[1] Institute of Space Sciences (ICE, CSIC), Campus UAB, Carrer de Can Magrans, s/n, 08193 Barcelona, Spain
[2] Institut d'Estudis Espacials de Catalunya (IEEC), Edifici RDIT, Campus UPC, 08860 Castelldefels, Barcelona, Spain
[3] INAF-Osservatorio Astronomico di Capodimonte, Via Moiariello 16, 80131 Napoli, Italy
[4] Max Planck Institute for Extraterrestrial Physics, Giessenbachstr. 1, 85748 Garching, Germany
[5] Dipartimento di Fisica e Astronomia, Università di Firenze, via G. Sansone 1, 50019 Sesto Fiorentino, Firenze, Italy
[6] University of Trento, Via Sommarive 14, I-38123 Trento, Italy
[7] INAF-Osservatorio Astrofisico di Arcetri, Largo E. Fermi 5, 50125, Firenze, Italy
[8] Instituto de Astrofísica de Canarias, E-38205 La Laguna, Tenerife, Spain
[9] Universidad de La Laguna, Dpto. Astrofísica, E-38206 La Laguna, Tenerife, Spain
[10] Institut de Ciencies de l'Espai (IEEC-CSIC), Campus UAB, Carrer de Can Magrans, s/n Cerdanyola del Vallés, 08193 Barcelona, Spain
[11] Department of Mathematics and Physics, Roma Tre University, Via della Vasca Navale 84, 00146 Rome, Italy
[12] INAF-Osservatorio Astronomico di Roma, Via Frascati 33, 00078 Monteporzio Catone, Italy
[13] School of Physics, HH Wills Physics Laboratory, University of Bristol, Tyndall Avenue, Bristol, BS8 1TL, UK
[14] Leiden Observatory, Leiden University, Einsteinweg 55, 2333 CC Leiden, The Netherlands
[15] INAF-Osservatorio Astronomico di Padova, Via dell'Osservatorio 5, 35122 Padova, Italy
[16] Universitäts-Sternwarte München, Fakultät für Physik, Ludwig-Maximilians-Universität München, Scheinerstr. 1, 81679 München, Germany
[17] Instituto de Física de Cantabria, Edificio Juan Jordá, Avenida de los Castros, 39005 Santander, Spain
[18] INAF-Osservatorio di Astrofisica e Scienza dello Spazio di Bologna, Via Piero Gobetti 93/3, 40129 Bologna, Italy
[19] Institute of Theoretical Astrophysics, University of Oslo, P.O. Box 1029 Blindern, 0315 Oslo, Norway
[20] INAF-Istituto di Astrofisica e Planetologia Spaziali, via del Fosso del Cavaliere, 100, 00100 Roma, Italy
[21] School of Physics & Astronomy, University of Southampton, Highfield Campus, Southampton SO17 1BJ, UK
[22] Jet Propulsion Laboratory, California Institute of Technology, 4800 Oak Grove Drive, Pasadena, CA, 91109, USA
[23] Department of Physics and Astronomy, University of Utah, 115 South 1400 East, Salt Lake City, UT 84112, USA
[24] Department of Physics and Helsinki Institute of Physics, Gustaf Hällströmin katu 2, University of Helsinki, 00014 Helsinki, Finland
[25] Department of Astronomy, University of Geneva, ch. d'Ecogia 16, 1290 Versoix, Switzerland
[26] ESAC/ESA, Camino Bajo del Castillo, s/n., Urb. Villafranca del Castillo, 28692 Villanueva de la Cañada, Madrid, Spain
[27] INAF-Osservatorio Astronomico di Brera, Via Brera 28, 20122 Milano, Italy
[28] Dipartimento di Fisica e Astronomia, Università di Bologna, Via Gobetti 93/2, 40129 Bologna, Italy
[29] INFN-Sezione di Bologna, Viale Berti Pichat 6/2, 40127 Bologna, Italy
[30] INAF-Osservatorio Astronomico di Trieste, Via G. B. Tiepolo 11, 34143 Trieste, Italy
[31] IFPU, Institute for Fundamental Physics of the Universe, via Beirut 2, 34151 Trieste, Italy
[32] Department of Physics "E. Pancini", University Federico II, Via Cinthia 6, 80126, Napoli, Italy
[33] Dipartimento di Fisica, Università degli Studi di Torino, Via P. Giuria 1, 10125 Torino, Italy
[34] INFN-Sezione di Torino, Via P. Giuria 1, 10125 Torino, Italy
[35] INAF-Osservatorio Astrofisico di Torino, Via Osservatorio 20, 10025 Pino Torinese (TO), Italy
[36] Institute for Astronomy, University of Edinburgh, Royal Observatory, Blackford Hill, Edinburgh EH9 3HJ, UK
[37] INAF-IASF Milano, Via Alfonso Corti 12, 20133 Milano, Italy
[38] Centro de Investigaciones Energéticas, Medioambientales y Tecnológicas (CIEMAT), Avenida Complutense 40, 28040 Madrid, Spain
[39] Port d'Informació Científica, Campus UAB, C. Albareda s/n, 08193 Bellaterra (Barcelona), Spain
[40] INFN section of Naples, Via Cinthia 6, 80126, Napoli, Italy
[41] Institute for Astronomy, University of Hawaii, 2680 Woodlawn Drive, Honolulu, HI 96822, USA
[42] Dipartimento di Fisica e Astronomia "Augusto Righi" - Alma Mater Studiorum Università di Bologna, Viale Berti Pichat 6/2, 40127 Bologna, Italy
[43] Jodrell Bank Centre for Astrophysics, Department of Physics and Astronomy, University of Manchester, Oxford Road, Manchester M13 9PL, UK
[44] European Space Agency/ESRIN, Largo Galileo Galilei 1, 00044 Frascati, Roma, Italy
[45] Université Claude Bernard Lyon 1, CNRS/IN2P3, IP2I Lyon, UMR 5822, Villeurbanne, F-69100, France
[46] Institut de Ciències del Cosmos (ICCUB), Universitat de Barcelona (IEEC-UB), Martí i Franquès 1, 08028 Barcelona, Spain
[47] Institució Catalana de Recerca i Estudis Avançats (ICREA), Passeig de Lluís Companys 23, 08010 Barcelona, Spain
[48] UCB Lyon 1, CNRS/IN2P3, IUF, IP2I Lyon, 4 rue Enrico Fermi, 69622 Villeurbanne, France
[49] Mullard Space Science Laboratory, University College London, Holmbury St Mary, Dorking, Surrey RH5 6NT, UK
[50] Université Paris-Saclay, CNRS, Institut d'astrophysique spatiale, 91405, Orsay, France
[51] Space Science Data Center, Italian Space Agency, via del Politecnico snc, 00133 Roma, Italy
[52] University Observatory, LMU Faculty of Physics, Scheinerstr. 1, 81679 Munich, Germany
[53] Department of Physics, Lancaster University, Lancaster, LA1 4YB, UK
[54] Felix Hormuth Engineering, Goethestr. 17, 69181 Leimen, Germany
[55] Technical University of Denmark, Elektrovej 327, 2800 Kgs. Lyngby, Denmark
[56] Cosmic Dawn Center (DAWN), Denmark
[57] Max-Planck-Institut für Astronomie, Königstuhl 17, 69117 Heidelberg, Germany
[58] NASA Goddard Space Flight Center, Greenbelt, MD 20771, USA
[59] Aix-Marseille Université, CNRS/IN2P3, CPPM, Marseille, France
[60] Université de Genève, Département de Physique Théorique and Centre for Astroparticle Physics, 24 quai Ernest-Ansermet, CH-1211 Genève 4, Switzerland
[61] Department of Physics, P.O. Box 64, University of Helsinki, 00014 Helsinki, Finland
[62] Helsinki Institute of Physics, Gustaf Hällströmin katu 2, University of Helsinki, 00014 Helsinki, Finland
[63] Laboratoire d'etude de l'Univers et des phenomenes eXtremes, Observatoire de Paris, Université PSL, Sorbonne Université, CNRS, 92190 Meudon, France
[64] SKAO, Jodrell Bank, Lower Withington, Macclesfield SK11 9FT, UK
[65] Centre de Calcul de l'IN2P3/CNRS, 21 avenue Pierre de Coubertin 69627 Villeurbanne Cedex, France
[66] Dipartimento di Fisica "Aldo Pontremoli", Università degli Studi di Milano, Via Celoria 16, 20133 Milano, Italy
[67] INFN-Sezione di Milano, Via Celoria 16, 20133 Milano, Italy

[68] Universität Bonn, Argelander-Institut für Astronomie, Auf dem Hügel 71, 53121 Bonn, Germany
[69] INFN-Sezione di Roma, Piazzale Aldo Moro, 2 - c/o Dipartimento di Fisica, Edificio G. Marconi, 00185 Roma, Italy
[70] Aix-Marseille Université, CNRS, CNES, LAM, Marseille, France
[71] Dipartimento di Fisica e Astronomia "Augusto Righi" - Alma Mater Studiorum Università di Bologna, via Piero Gobetti 93/2, 40129 Bologna, Italy
[72] Department of Physics, Institute for Computational Cosmology, Durham University, South Road, Durham, DH1 3LE, UK
[73] Université Paris Cité, CNRS, Astroparticule et Cosmologie, 75013 Paris, France
[74] CNRS-UCB International Research Laboratory, Centre Pierre Binétruy, IRL2007, CPB-IN2P3, Berkeley, USA
[75] Institut d'Astrophysique de Paris, 98bis Boulevard Arago, 75014, Paris, France
[76] Institut d'Astrophysique de Paris, UMR 7095, CNRS, and Sorbonne Université, 98 bis boulevard Arago, 75014 Paris, France
[77] Institute of Physics, Laboratory of Astrophysics, Ecole Polytechnique Fédérale de Lausanne (EPFL), Observatoire de Sauverny, 1290 Versoix, Switzerland
[78] Telespazio UK S.L. for European Space Agency (ESA), Camino bajo del Castillo, s/n, Urbanizacion Villafranca del Castillo, Villanueva de la Cañada, 28692 Madrid, Spain
[79] Institut de Física d'Altes Energies (IFAE), The Barcelona Institute of Science and Technology, Campus UAB, 08193 Bellaterra (Barcelona), Spain
[80] School of Mathematics and Physics, University of Surrey, Guildford, Surrey, GU2 7XH, UK
[81] European Space Agency/ESTEC, Keplerlaan 1, 2201 AZ Noordwijk, The Netherlands
[82] DARK, Niels Bohr Institute, University of Copenhagen, Jagtvej 155, 2200 Copenhagen, Denmark
[83] Waterloo Centre for Astrophysics, University of Waterloo, Waterloo, Ontario N2L 3G1, Canada
[84] Department of Physics and Astronomy, University of Waterloo, Waterloo, Ontario N2L 3G1, Canada
[85] Perimeter Institute for Theoretical Physics, Waterloo, Ontario N2L 2Y5, Canada
[86] Université Paris-Saclay, Université Paris Cité, CEA, CNRS, AIM, 91191, Gif-sur-Yvette, France
[87] Centre National d'Etudes Spatiales – Centre spatial de Toulouse, 18 avenue Edouard Belin, 31401 Toulouse Cedex 9, France
[88] Institute of Space Science, Str. Atomistilor, nr. 409 Măgurele, Ilfov, 077125, Romania
[89] Dipartimento di Fisica e Astronomia "G. Galilei", Università di Padova, Via Marzolo 8, 35131 Padova, Italy
[90] INFN-Padova, Via Marzolo 8, 35131 Padova, Italy
[91] Caltech/IPAC, 1200 E. California Blvd., Pasadena, CA 91125, USA
[92] Institut für Theoretische Physik, University of Heidelberg, Philosophenweg 16, 69120 Heidelberg, Germany
[93] Institut de Recherche en Astrophysique et Planétologie (IRAP), Université de Toulouse, CNRS, UPS, CNES, 14 Av. Edouard Belin, 31400 Toulouse, France
[94] Université St Joseph; Faculty of Sciences, Beirut, Lebanon
[95] Departamento de Física, FCFM, Universidad de Chile, Blanco Encalada 2008, Santiago, Chile
[96] Satlantis, University Science Park, Sede Bld 48940, Leioa-Bilbao, Spain
[97] Departamento de Física, Faculdade de Ciências, Universidade de Lisboa, Edifício C8, Campo Grande, PT1749-016 Lisboa, Portugal
[98] Instituto de Astrofísica e Ciências do Espaço, Faculdade de Ciências, Universidade de Lisboa, Tapada da Ajuda, 1349-018 Lisboa, Portugal
[99] Cosmic Dawn Center (DAWN)
[100] Niels Bohr Institute, University of Copenhagen, Jagtvej 128, 2200 Copenhagen, Denmark
[101] Universidad Politécnica de Cartagena, Departamento de Electrónica y Tecnología de Computadoras, Plaza del Hospital 1, 30202 Cartagena, Spain
[102] INFN-Bologna, Via Irnerio 46, 40126 Bologna, Italy
[103] Astronomisches Rechen-Institut, Zentrum für Astronomie der Universität Heidelberg, Mönchhofstr. 12-14, 69120 Heidelberg, Germany
[104] Instituto de Física Teórica UAM-CSIC, Campus de Cantoblanco, 28049 Madrid, Spain
[105] Université PSL, Observatoire de Paris, Sorbonne Université, CNRS, LERMA, 75014, Paris, France
[106] Université Paris-Cité, 5 Rue Thomas Mann, 75013, Paris, France
[107] Univ. Grenoble Alpes, CNRS, Grenoble INP, LPSC-IN2P3, 53, Avenue des Martyrs, 38000, Grenoble, France
[108] Aurora Technology for European Space Agency (ESA), Camino bajo del Castillo, s/n, Urbanizacion Villafranca del Castillo, Villanueva de la Cañada, 28692 Madrid, Spain
[109] ICL, Junia, Université Catholique de Lille, LITL, 59000 Lille, France

Appendix A: DESI fiber collisions

DESI fibers are limited by the "patrol radius" of the positioners, which results in insufficient available fibers when covering densely populated regions of the sky. Additionally, the physical size of the positioner limits the minimum angular separation between two optical fibers, which means that two (or more) sources with small angular separations cannot be observed simultaneously. Since the combination of these effects is effectively similar to the fiber collisions in SDSS, this issue is also referred to as fiber collisions (Bianchi et al. 2025). A direct consequence of missing closely separated sources is the undercount of physically close pairs, which we estimate here taking an empirical approach.

First we measure the spectroscopic completeness of DESI EDR in the *Euclid*-DESI crossmatch region using two catalogues: the DESI EDR (the observed catalogue) and the Legacy Survey DR9 photometry value-added catalogue of potential targets list (the parent catalogue), which contains all the targets that DESI could have observed (DESI Collaboration et al. 2024). Even after restricting the observed and parent catalogues to the *Euclid*-DESI crossmatch region (12.5 deg^2), the large amount of sources in both catalogues (especially the parent) makes it impractical to directly measure the number of pairs as a function of angular separation. Instead, we sample 60 different circular subregions of ∼0.061 deg^2, each of which can contain pairs with up to 1000″ in angular separation. For each region we derive the number of potential $n_{\rm pot}(\theta_i)$ and observed $n_{\rm obs}(\theta_i)$ targets per angular separation bin θ_i. We also derive the number $n_{\rm phys}(\theta_i)$ of actual physical pairs (as defined in Sect. 2.1) per angular bin to calculate the probability that an observed pair is a physical pair as a function of the angular separation as

$$p_{\rm phys}(\theta_i) = \frac{n_{\rm phys}(\theta_i)}{n_{\rm obs}(\theta_i)} \, . \tag{A.1}$$

Then we use $p_{\rm phys}(\theta_i)$ to estimate the number of physical missing pairs as

$$n^{l}_{\rm phys\_miss}(\theta_i) = p_{\rm phys}(\theta_i)\, n_{\rm miss}(\theta_i) \, , \tag{A.2}$$

where $n_{\rm miss}(\theta_i) = n_{\rm pot}(\theta_i) - n_{\rm obs}(\theta_i)$. We can consider $n^{l}_{\rm phys\_miss}(\theta_i)$ (and all quantities derived from it) as a lower limit (denoted by the superindex l) because $p_{\rm phys}(\theta_i)$ was obtained assuming that the probabilities of a pair being observed and a pair being physical are independent. However, since physical pairs are more likely to be found in denser regions, they have a lower chance of being observed than random pairs at the same angular separation. This means that $n_{\rm phys\_miss}(\theta_i)$ might be an underestimate of the actual missing physical pairs. To obtain a more conservative limit, we apply the correction

$$p^{\rm corr}_{\rm phys}(\theta_i) = \min\left(1, \frac{p_{\rm phys}(\theta_i)}{C(\theta_i)}\right) \, , \tag{A.3}$$

where $C(\theta_i) = n_{\rm obs}(\theta_i)/n_{\rm pot}(\theta_i)$ is the pair completeness as a function of angular separation, and we use the min() function to ensure the probability is never greater than 1. Then

$$n^{u}_{\rm phys\_miss}(\theta_i) = p^{\rm corr}_{\rm phys}(\theta_i)\, n_{\rm miss}(\theta_i) \, . \tag{A.4}$$

After going over all the sample regions, we combine the counts to obtain the spectroscopic pair completeness as a function of angular separation, which is shown in Fig. A.1. The effect of fiber collision becomes apparent as a decline in completeness from ∼ 200″ towards smaller separations.

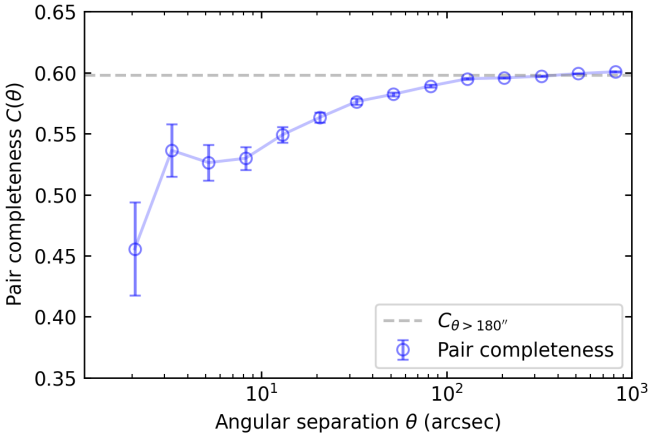

Fig. A.1. Spectroscopic pair completeness of DESI EDR vs. pair angular separation for the 60 sample regions taken from the DESI-*Euclid* crossmatch. The grey dashed line is the average completeness for all pairs with θ>180″. The vertical bars represent the binomial error of each bin.

We estimate the relative portion of missing pairs due to fiber collision as

$$f_{\rm miss\_fc}(\theta_i) = C_{\theta>180''} - C(\theta_i) \, , \tag{A.5}$$

where $C_{\theta>180''}$ is the average pair completeness for pairs with $\theta >$ 180″, since at those separations we can expect the fiber collision incompleteness to be negligible (e.g. Pinon et al. 2025). We then estimate the number of physical pairs due to fiber collisions as

$$n^{b}_{\rm miss\_fc}(\theta_i) = \frac{f_{\rm miss\_fc}(\theta_i)}{f_{\rm obs\_miss}(\theta_i)}\, n^{b}_{\rm phys\_miss}(\theta_i) \, , \tag{A.6}$$

where $f_{\rm obs\_miss}(\theta_i) = 1 - C(\theta_i)$, and the superindex b can be either u or l to get the upper or lower limits, respectively. Finally, we obtain the fraction of missing physical pairs as

$$f^{b}_{\rm phys\_miss\_fc} = \frac{1}{C_{\theta>180''}} \frac{\sum_{i=0}^{n_{\rm bin}} n^{b}_{\rm miss\_fc}(\theta_i)}{\sum_{i=0}^{n_{\rm bin}} [n_{\rm phys\_obs}(\theta_i) + n^{b}_{\rm phys\_miss}(\theta_i)]} \, , \tag{A.7}$$

where $n_{\rm phys\_obs}(\theta_i)$ is the number of observed physical pairs per angular bin, $n_{\rm bin}$ is the number of angular separation bins, and we use $C_{\theta>180''}$ to scale $f^{b}_{\rm phys\_miss\_fc}$ to obtain the missing pair fraction exclusively due to fiber collision.

Appendix B: SED fitting

Two examples of the SED fitting performed by `CIGALE` are shown in Fig. B.1.

Appendix C: Radio counterparts

The eight LOFAR sources in the sample of dual AGN candidates in low-mass galaxies are included in the Bisigello et al. (2025) catalogue, which includes optical-to-near-infrared counterparts for 99.2% of the LOFAR sources presented in the catalogue

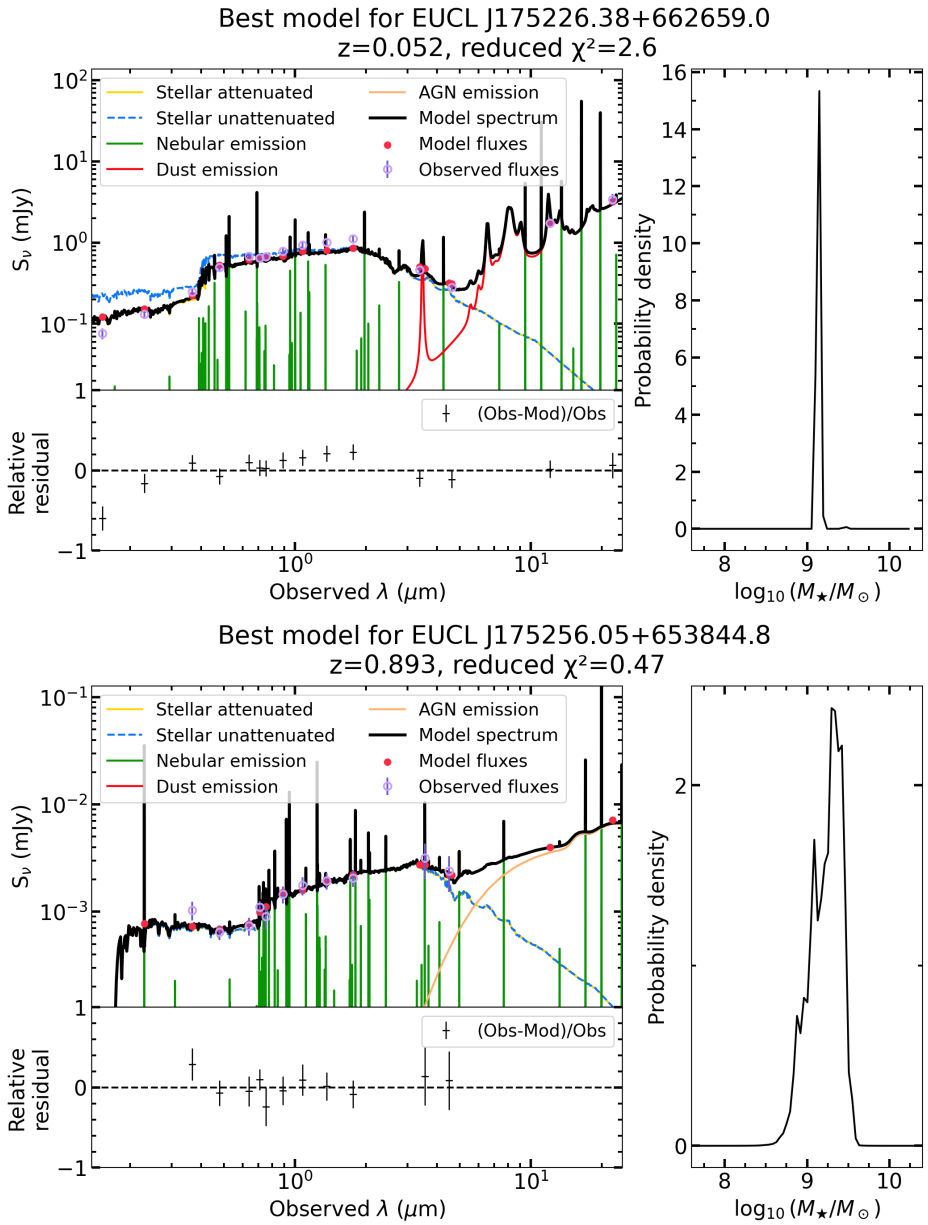

Fig. B.1. Examples of CIGALE best-fit SED models (black line) for one of the galaxies in a low-redshift dual AGN system (*top panel*) and a high-redshift one (*bottom panel*). The observed fluxes in the different bands are shown by purple circles, while the best-fit modelled fluxes in these bands are represented by red dots. The different coloured lines correspond to the various SED components. For each source, a side panel displays the M_* probability distribution function returned by CIGALE, showcasing their low-mass nature.

Table B.1. Total and peak radio fluxes, and total radio luminosity at a central frequency of 144 MHz for those sources in the sample of dual AGN candidates in low-mass galaxies with an AGN radio counterpart.

IAU Name	$S_{\rm tot}$ (mJy)	$S_{\rm peak}$ (mJy)	$\log_{10}(L_{144\,\rm MHz}/\rm W\ Hz^{-1})$
EUCL J174726.73+662605.0	0.9 ± 0.2	0.33 ± 0.05	22.66 ± 0.08
EUCL J174727.18+662623.6	0.8 ± 0.1	0.85 ± 0.04	22.64 ± 0.04
EUCL J175226.38+662659.0	1.2 ± 0.1	0.80 ± 0.04	21.90 ± 0.03
EUCL J175228.85+662646.8	0.4 ± 0.1	0.22 ± 0.04	21.4 ± 0.1
EUCL J180150.12+670229.9	0.7 ± 0.2	0.23 ± 0.04	22.1 ± 0.1
EUCL J180154.58+670240.4	0.8 ± 0.1	0.39 ± 0.04	22.16 ± 0.07
EUCL J181025.14+664252.8	1.3 ± 0.1	0.92 ± 0.05	22.39 ± 0.04
EUCL J181026.79+664235.5	0.6 ± 0.1	0.29 ± 0.05	22.0 ± 0.1

by Bondi et al. (2024), excluding masked sources. Counterparts are identified using the likelihood ratio method (de Ruiter et al. 1977; Sutherland & Saunders 1992) based on both the magnitude and colour information, using the optical Subaru Hyper

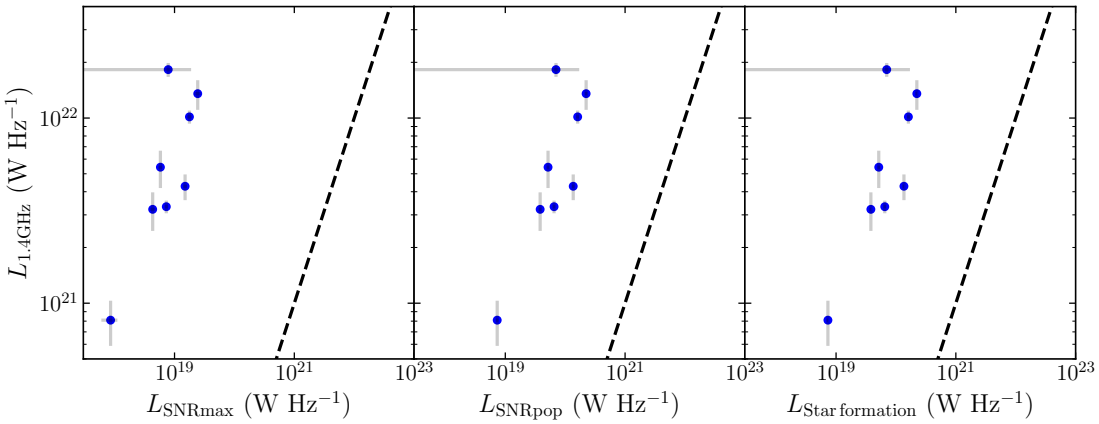

Fig. B.2. Radio luminosity at 1.4 GHz of those dual AGN candidates in low-mass galaxies with a LOFAR radio counterpart versus expected radio luminosity from bright SNe and SNRs (*left*), from a population of SNe/SNRs (*middle*), and from star formation (*right*). The dashed lines denote one-to-one correlations.

Suprime-Cam (HSC) *i*-band and the 4.5-μm *Spitzer*/IRAC band. Cross-matches for the most complex sources have been validated with visual inspection by two independent researchers. Given the high success rate of identifications, we directly crossmatch our *Euclid* sources with the optical-to-near-infrared positions of the LOFAR counterparts using a matching radius of 1″. We estimate the contamination fraction of the crossmatch based on the number density of LOFAR in the coverage of the EDF-N (23,309 LOFAR objects over 10 deg^2; Bisigello et al. 2025) and that of *Euclid* EDF-N in that area (285,111 objects/deg^2). Using a blunder radius of 1.″0, we find 1611 random matches and derive a contamination fraction of 8.3%. Yet, all eight *Euclid* sources with a LOFAR counterpart are confirmed as the most probable counterpart based on the likelihood ratio analysis presented in Bisigello et al. (2025), with a likelihood ratio at least 100 times larger than the threshold above which a counterpart is considered valid, as derived from the entire LOFAR sample. Using the method described by Nisbet (2018) and Kondapally et al. (2021), this likelihood ratio corresponds to a probability of a source being a genuine counterpart above 99.4%.

The LOFAR data were taken at a frequency of 144 MHz and the image has an angular resolution of 6″. The root mean square of the LOFAR images ranges from 0.04 to 0.06 mJy beam^{-1}. The radio source catalogue was extracted by Bondi et al. (2024) using the Python Blob Detection and Source Finder (`PyBDSF`, Mohan & Rafferty 2015). The coordinate-based IAU name and fluxes of the eight radio sources were retrieved from this catalogue and are provided in Table B.1. To compute the radio luminosity at 1.4 GHz and compare it to that expected from stellar processes, we assume a radio spectral index α typical of AGNs, $\alpha = 0.7$ and $S_\nu \propto \nu^{-\alpha}$, where S_ν is the radio flux at frequency ν. We use the SED-based star-formation rate of each galaxy to compute the expected contribution at 1.4 GHz from bright supernovae (SNe) and supernova remnants (SNRs), a population of SNe/SNRs, and from star formation to the radio emission following Reines et al. (2020) and Flores et al. (2025). A source is then classified as an AGN when its radio luminosity is at least three times larger than the luminosity predicted from these stellar processes, including their uncertainties (see Fig. B.2). On the basis of this comparison, we conclude that the radio emission is due to AGN phenomena in all the eight objects.

Appendix D: *Euclid* spectral fitting

In this appendix, we present the results of fitting the *Euclid* spectra for the source discussed in Sect. 3.2. The spectrum of EUCL J174727.18+662623.6 is shown in Fig. D.1, with emission lines fitted using the method described in Sect. 2.2. We mask regions affected by instrumental features or high noise and we use the DESI spectroscopic redshift to perform the emission line fitting of the *Euclid* spectra. The observed data are plotted in black, while the best-fit model is overlaid in red. The model comprises a power-law continuum and Gaussian emission lines, including both broad and narrow components as required. Individual fit components are displayed in different colours, with the continuum shown in blue. To improve the robustness of the fit, we adopt a physically motivated strategy for the line widths: the narrow lines, which originate from the narrow-line region (NLR), are assumed to have a common velocity dispersion and are therefore fitted with the same fixed width. Similarly, broad lines associated with the broad-line region (BLR) are tied together in width, but allowed to vary independently from the NLR. This approach reduces degeneracies between line fluxes and widths, ensures that the fitted components reflect the expected kinematics of the emitting regions, and prevents unphysical variations in width for lines arising from the same physical region. The fluxes and FWHMs of the fitted *Euclid* emission lines are listed in Table D.1. We adopt a conservative 20% uncertainty on the flux measurements of the main emission lines, accounting for both fitting and calibration errors. We fit and report the fluxes and FWHMs only for lines with S/N $\geq$ 5.

We compute the black hole mass based on the FWHM and luminosity of the (Paβ)$_\mathrm{b}$ and (He I λ 1.084)$_\mathrm{b}$. For Paβ we use Equation (7) in La Franca et al. (2015), adding a $\log_{10}(5.5/4.31)$ term to re-scale the geometrical factor from 4.31 to 5.5 (equivalent to $\epsilon = 1$):

$$\log_{10}\left(\frac{M_{\mathrm{BH}}}{M_\odot}\right) = 7.83 + \log_{10}\left(\frac{5.5}{4.31}\right) + 0.872\left[2\log_{10}(\mathrm{FWHM}) + 0.5\log_{10}\left(L_{\mathrm{Pa}\beta}\right)\right], \quad \text{(D.1)}$$

where FWHM is that of (Paβ)$_\mathrm{b}$ in units of 10^4 km s^{-1} and $L_{\mathrm{Pa}\beta}$ is the (Paβ)$_\mathrm{b}$ line luminosity in units of 10^{40} erg s^{-1}.

For He I we take the relation from Ricci et al. (2017):

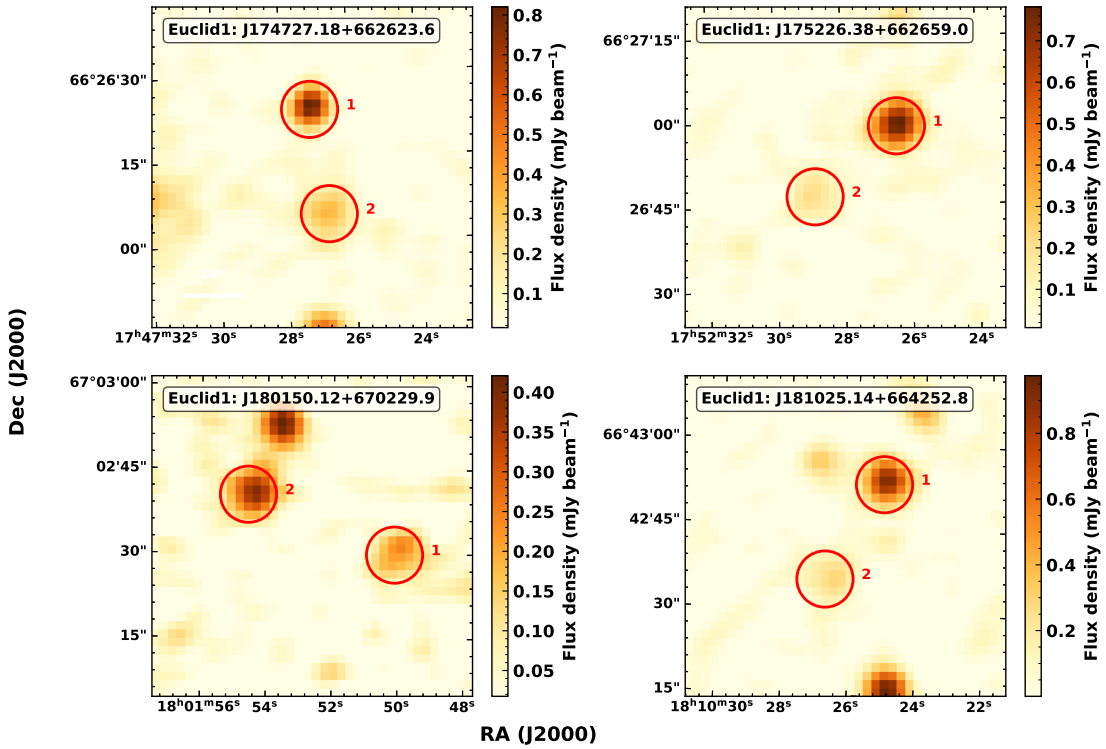

Fig. C.1. LOFAR EDF-N radio images at 144 MHz with a resolution of 6″ for those dual AGNs in low-mass galaxies with a LOFAR radio counterpart. The red circles mark the positions of the AGNs, as in Fig. 3.

$$\log_{10}\left(\frac{M_{\rm BH}}{M_\odot}\right) = 7.75 + \log_{10}\left(\frac{5.5}{4.31}\right) + 2\,\log_{10}({\rm FWHM}) + 0.5\log_{10}\left(\frac{L_{14-195\,{\rm keV}}}{10^{42}}\right), \quad (D.2)$$

where FWHM is that of (He I λ 1.084)$_{\rm b}$ in units of 10^4 km s^{-1} and $L_{14-195\,{\rm keV}}$ is the 14–195 keV hard-X luminosity in units erg s^{-1}. We then re-scale the $L_{14-195\,{\rm keV}}$ to that of He I using the value reported in Ricci et al. (2022):

$$\log_{10}(L_{\rm He\,I}) = \log_{10}(L_{14-195\,{\rm keV}}) - 2.45, \quad (D.3)$$

where $L_{\rm He\,I}$ is the (He I λ 1.084)$_{\rm b}$ luminosity in erg s^{-1}.

Combining Eqs.(D.2) and (D.3), we obtain:

$$\log_{10}\left(\frac{M_{\rm BH}}{M_\odot}\right) = 7.86 + 2\,\log_{10}({\rm FWHM}) + 0.5\,\left[\log_{10}(L_{\rm He\,I}) - 39.55\right], \quad (D.4)$$

where FWHM is that of (He I λ 1.084)$_{\rm b}$ in units of 10^4 km s^{-1}.

Appendix E: DESI spectroscopy

We visually inspect each individual DESI EDR spectrum of the 18 AGN candidates forming the sample of nine dual AGNs in low-mass galaxies, ensuring that there are no artifacts affecting the emission lines used in the diagnostic diagrams. We show here two examples of the DESI EDR spectra: for the galaxy at $z \simeq 0.14$ with broad Hα emission (EUCL J174727.18+662623.6; Fig. E.1, top,) and for one of the galaxies at $z \simeq 0.9$ with an AGN classification based on the BLUE and KEX diagrams (EUCL J175759.76+654524.6; Fig. E.1, bottom). The remaining spectra can be downloaded from the DESI EDR website. In Figs. E.2 to E.4 we also show the N II-BPT, S II-BPT, WHAN, BLUE, and KEX emission-line diagnostics of the sources classified as AGNs based on DESI spectroscopy (see also Table 1).

Table D.1. Fluxes and FWHM values of emission lines detected in EUCL J174727.18+662623.6.

Line ID	Flux [10^{-16} erg s^{-1} cm^{-2}]	FWHM [km s^{-1}]
(He I λ 1.084)$_{\rm b}$	15 ± 3	5083 ± 1000
(He I λ 1.083)$_{\rm n}$	13 ± 3	1469 ± 290
Paγ	5.0 ± 1.0	1469 ± 290
[O I] λ 1.129	4.7 ± 0.9	1469 ± 290
(Paβ)$_{\rm b}$	16 ± 3	5083 ± 1000
(Paβ)$_{\rm n}$	6.5 ± 1.3	1469 ± 290

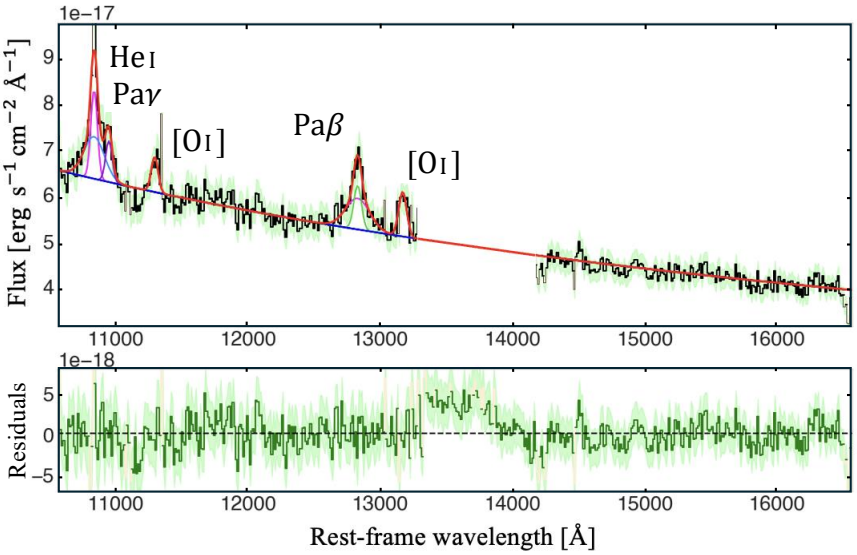

Fig. D.1. *Euclid* spectrum of EUCL J174727.18+662623.6. The spectrum is shown in black, with the best-fit model overplotted in red. Spectral regions affected by instrumental artefacts or elevated noise levels are masked. The fit includes a power-law continuum (in blue) and emission lines, represented in different colours depending on the component. The main lines are labelled in the plot. The bottom panel displays the residuals between the data and the model. The fitting procedure is described in detail in Appendix D.

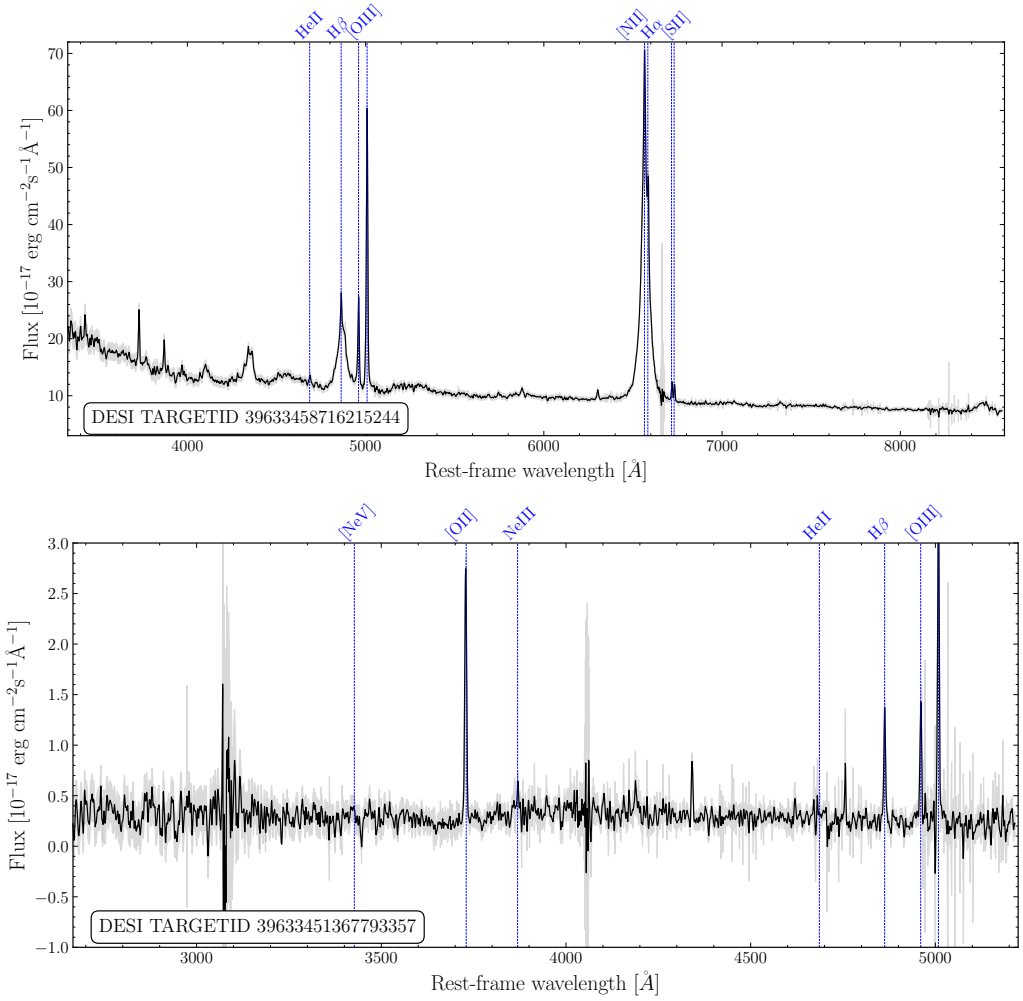

Fig. E.1. Two examples of the DESI spectra (black line) for dual AGNs in low-mass galaxies: EUCL J174727.18+662623.6 (*top*), at $z \simeq 0.14$ showing clear broad Hα emission; and EUCL J175759.76+654524.6 (*bottom*), at $z \simeq 0.9$ classified as an AGNs based on the BLUE and KEX diagrams. The 1σ uncertainty of the flux is shown as a grey line. The blue vertical lines mark the position of those emission lines typically used for AGN classification.

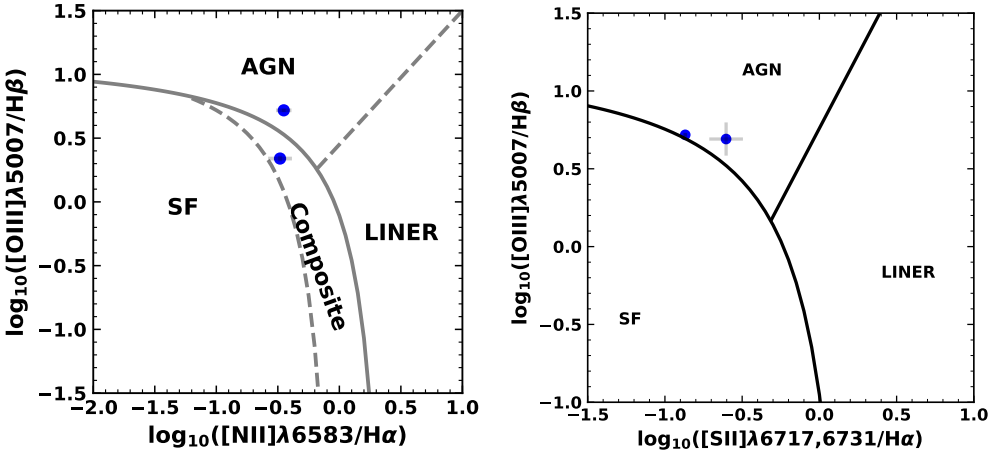

Fig. E.2. N II-BPT (*left*) and S II-BPT (*right*) diagram of those sources classified as AGNs in one of these diagnostics based on DESI spectroscopy. In the N II-BPT, the solid line delineates the regions corresponding to AGN and star formation (SF) from Kewley et al. (2001), while the dashed lines delineate those regions corresponding to SF and composite (combination of AGNs and SF) from Kauffmann et al. (2003), and those corresponding to AGNs vs. low-ionisation nuclear emission-line region (LINER) emission from Schawinski et al. (2007). In the S II-BPT, the solid lines delineate the regions corresponding to AGNs and SF from Kewley et al. (2001) and those corresponding to AGN vs. LINER emission from Schawinski et al. (2007).

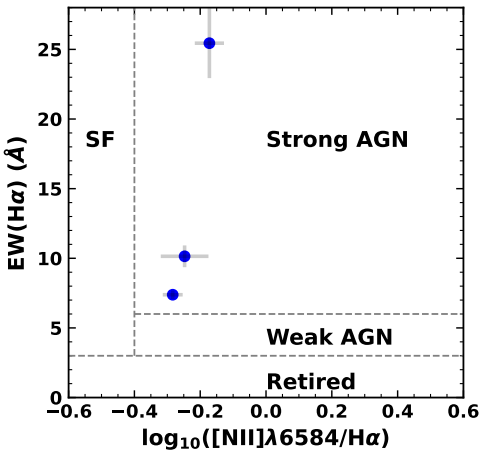

Fig. E.3. WHAN diagram of those sources classified as AGNs in this diagnostic based on DESI spectroscopy. The dashed lines separate regions dominated by strong and weak AGN emission, SF emission, and Retired galaxies as defined by Cid Fernandes et al. (2010).

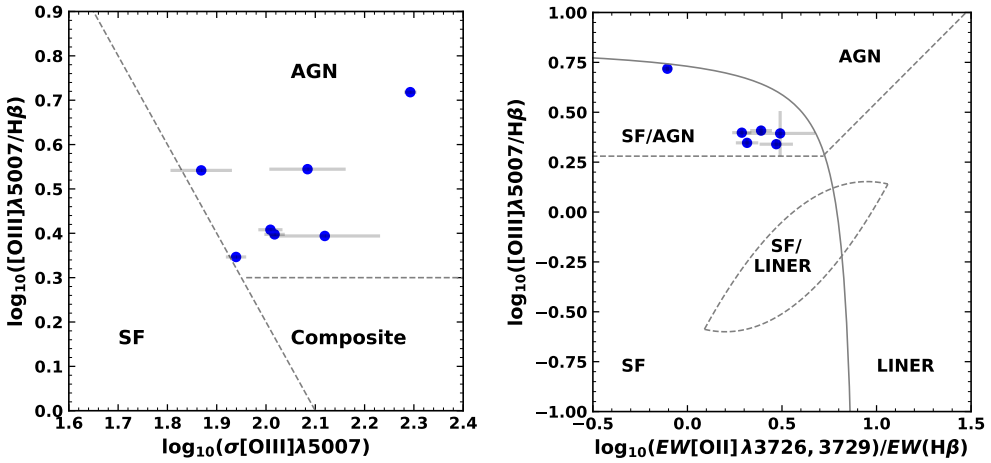

Fig. E.4. KEX (*left*) and BLUE (*right*) diagrams of those sources classified as AGNs in one of these diagnostics based on DESI spectroscopy. In the KEX diagram, the dashed lines delineate the regions corresponding to AGNs, SF, and composite (combination of AGNs and SF) emission based on Zhang & Hao (2018). In the BLUE diagram, the dashed lines indicate regions dominated by AGNs, SF, a combination of SF and AGNs (SF/AGN), LINER, and a combination of SF and LINER (SF/LINER) emission based on Lamareille (2010).